



Final Report on contract W7701-102465/001/QCL **“Energetic Characterization of Metal-Hybrid Fuels”**

By

Drs. Sam Goroshin, Jeffrey Bergthorson, David Frost, Andrew Higgins and
Yinon Yavor

Contract Project Manager: Dr. Sam Goroshin, 514-398-3262

PWGSC Contract Number: W7701-102465/001/QCL

CSA: Dr. Robert Stowe, Weapons Systems Section, 418-844-4000 ext 4318

Montreal,
March 31st 2013

Synopsis

The research work under the current contract was concentrated around two major directions: a) study of the different aspects of boron combustion and b) investigation of the aluminum-water reaction and combustion.

A). Elemental boron, having the highest volumetric energy density among all elements has long been considered as an attractive fuel for air-breathing propulsion. However, due to complex chemistry, high ignition temperature and long combustion time, the practical utilization of boron in realistic fuel compositions and devices has proved to be difficult. Under the current contract, we have continued the study of the ignition of boron particle agglomerates initiated under the previous DRDC contracts. Agglomeration of particles, often observed in various propulsion systems utilizing metal fuel, has always been viewed as a purely deleterious phenomenon that increases combustion time of the fuel and frequently leads to a loss in specific impulse. As shown in the current work, this negative effect can be offset, at least partially, by a drastic reduction in the ignition temperature of the agglomerate in comparison to a single particle. Thus, for boron, whose high ignition temperature was always considered detrimental for efficient utilization, the reduction in ignition temperature observed with agglomerates in comparison to single particles can exceed 1000 K. The ignition of the boron agglomerate as shown both experimentally and theoretically in the present work, is a dual stage phenomenon resulting from a complex interplay between boron oxidation, evaporation of the oxide, and diffusion of oxygen towards the large internal agglomerate surface area. Because of the large reactive surface area, the first ignition stage of the agglomerate occurs at relatively low temperatures when evaporation of the boron oxide is practically negligible. The build-up of the boron oxide inside the agglomerate during the first stage ignition process eventually blocks diffusion delivery of oxygen towards the agglomerate internal surface and may result in agglomerate quenching. However, if the peak temperature reached during the first ignition stage is sufficiently high, the rapid evaporation of the oxide eventually unblocks the internal surface for reaction providing conditions for the second stage ignition. The second ignition stage results in complete evaporation of the oxide from both external and internal surfaces of the agglomerate, resulting in transition to agglomerate combustion controlled by diffusion external to the agglomerate.

A simple way to facilitate boron combustion is to combine it with a more reactive constituent such as, for example, aluminum in a form of a binary mechanical mixture of corresponding powders. The more reactive metal component of the fuel (aluminum) will raise the temperature of the flow thus theoretically allowing for faster heterogeneous boron reactions. Such a blended fuel though having lower theoretical performance in comparison to fuel based on pure elementary boron may, nevertheless, in practice exceed performance of the compositions based on pure boron due to more efficient boron combustion. The current study of boron aluminum flame in products of the hydrocarbon (methane) combustion was performed on the apparatus “hybrid flame burner”. Analogous to the stabilization in a ducted rocket of metalized fuel, a laminar flow of metal powder suspension entrained in hydrocarbon-air mixture has the ability to sustain a Bunsen flame on a nozzle. We have confirmed possibility of stabilization of the dust flame in suspension of 85% of aluminum (Valimet H-5) and 15% of amorphous boron powder. Spectroscopic analysis of the flame showing presence of molecular band of intermediate boron oxides and flame temperatures deduced from the continuous part of the spectra provide indication to a fully developed boron combustion.

B) The aluminum-water reaction has been widely investigated over the years. In most cases, studies focused on the combustion process of aluminum and steam in two major areas: underwater propulsion technology and the high-temperature aluminum combustion in solid propellants. During the past few years, other applications of metal-water reactions have emerged, including aluminum-water “green” propellants which possess a specific impulse of around 230 s. These propellants can be used in various fields, and are most prominent in the area of space propulsion due to the light hydrogen gas produced during combustion. In combustion-related applications, however, only the thermal part of the energy associated to Al-water reaction is typically used (around 55%), while hydrogen serves merely as the exhaust gas.

For the last decade, another high-profile application of the metal water reaction has emerged: in-situ hydrogen generation, which can be utilized in fuel cells, generators and other devices. This topic has gained growing interest due to global climate change and the need for a clean, non-polluting fuel to replace hydrocarbons. Typically, the devices are operated under atmospheric pressures and at temperatures below the

boiling point of water, thus only the hydrogen-air reaction energy is used, and the thermal energy released in the aluminum-water reaction is lost. Efficient use of metal as an energy carrier requires harvesting the maximum energy that aluminum-water reaction can deliver utilizing both the hydrogen and the thermal energy released during its generation. In order to harness the heat generated during hydrogen production (using a steam turbine, thermoelectric (TE) generator or an externally-heated Stirling-type engine) the reaction has to be performed at temperatures considerably higher than the environment. While the aluminum-water combustion temperature (~3000 K) cannot be handled efficiently in practical devices, reactors operated at several hundred degrees can be designed and used, though elevated pressures are required in order to prevent the water from boiling. However, very limited data are available for the Al-water kinetics in the intermediate temperature regime, and therefore no reliable estimations on the feasibility and performance of such reactors have been published.

This study seeks to broaden our understanding of aluminum-water reactions over the temperature range from 20°C to 200°C, where hydrogen production is accompanied by possible utilization of the heat of the reaction. The reaction of aluminum powders with liquid distilled water was investigated for three spherical aluminum powders (ALEX, H-2 and H-10) with average particle sizes of 0.12, 6.0 and 13.8 microns, respectively. Experiments were performed in a batch-type reactor, at temperatures ranging from 20°C to 200°C and corresponding pressures of up to 2 MPa. The results show that, as reaction temperature increases, both the hydrogen production rate and total hydrogen yield increase. It was also demonstrated that a smaller-diameter powder reacted more quickly, had a higher hydrogen production rate, and produced a greater total yield of hydrogen throughout the temperature range. Hydrogen production rate per surface area was found to be independent of particle size, and an Arrhenius-type expression was derived for its temperature dependency. The estimated activation energy of the overall reaction was calculated to be 41.0 kJ/mol. Ultrasound experiments were conducted with various powders at temperatures as high as 90°C. The ultrasonic agitation resulted in increased hydrogen production rate, as well as in total hydrogen yield. The observed inhibitive mechanism for hydrogen production led to the introduction of a parameter, termed the penetration thickness, which represents the maximal hydrated layer thickness in an aluminum particle. It was shown that, penetration thickness increases with temperature and has little or no dependency on particle size.

The dependence of the burning rate on pressure of aluminum-water propellants containing different nano-size powders was investigated in order to study and characterize their properties. Three nano aluminum powders were examined: uncoated (U-ALEX, which includes the protective oxide layer), Palmitic acid coated (L-ALEX) and Viton coated (V-ALEX). It was found that all investigated compositions demonstrate increase in the burning rate with pressure in the pressure range below 3000 psi while the smallest pressure exponent was demonstrated by propellant with Viton coated nano-aluminum. However, all compositions have demonstrated a rapid decrease in burning rate at 3500 psi pressure that can be possibly associated with change of the propellant combustion regime above the critical point of water (3206 psi, 647 K).

We have also theoretically evaluated the possible use of metal-water composition as a gun propellant. A quasi-one-dimensional Lagrangian ballistics code has been developed in order to model the internal ballistics of a water-aluminum light gas gun. Using the information from the chemical equilibrium software calculations has indicate projectile speeds above 4 km/s for realistic projectile densities and driving gas mass/projectile mass ratios. This is well above the capacity of powder guns, which are limited to approximately 2.5 km/s for the same launching conditions.

The other work that was initiated in the course of the current contract includes study of metal-water reaction at supercritical conditions and development of the flame temperature measurement technique using an “atomic tracers” method (atomic lines thermometry), building and testing apparatus of for observing of the hybrid (metal-hydrocarbon) flame propagation and quenching in vertical tubes and the conceptual design of the high-pressure strand burner with the optical access.

Acknowledgements

McGill graduate and undergraduate students that have provided contribution to the current work:

Jennifer Sidey – experimental investigation of aluminum-water reactions

XiaoChen Mi – theoretical model for ignition of boron particle agglomerates

Michael Soo and **Philippe Julien** – experimental work on boron-aluminum-methane flames

William Georges – experimental work on high-pressure aluminum-water reaction and experiments on a strand burner with aluminum-water propellant

Jason Loiseau and **Jimmy Huneault** – theoretical calculations of the performance of aluminum-water light gas gun propellant

Mathew Burbaki, Oran Petel, Mathew Julien, Alexander Coderre-Chabot - assistance with design and construction of various set ups and diagnostics

Contents

Synopsis	2
Acknowledgements	4
Chapter I. Dual-stage ignition of boron particle agglomerates	7
Nomenclature.....	7
1. Introduction	8
2. Experimental details	9
2.1 Boron powders	9
2.2 Agglomerate preparation	10
2.3 Flow and heating	10
2.4 Optical diagnostics.....	11
3. Experimental.....	12
3.1 Two-stage agglomerate ignition phenomenon	12
3.2 Boron agglomerates ignition characteristics in wet flows	14
3.3 Boron agglomerate ignition characteristics in dry flows.....	15
4. Physical model of boron agglomerate ignition	16
4.1 Model Objectives.....	16
4.2 Model assumptions	16
4.3 Layered agglomerate ignition model and its governing equations.....	18
4.4 Theoretical results, comparison with the experiment, and discussion.....	20
5. Conclusion	22
References to the Chapter I.....	23
Chapter II. Combustion of Boron-Aluminum suspension in products of the hydrocarbon flame	24
1.1 Introduction.....	24
1.2 Boron Mixtures.....	24
2.1 Boron-aluminum-26% O ₂ flame	25
2.3Flames in Boron-aluminum-CH ₄ -26% O ₂ mixtures	26
2.3.1 Flame speed.....	28
2.3.2. Combustion product analysis	29
2.3.3Thermodynamic Analysis.....	29
References to Chapter II	30
Chapter III. Enhanced Hydrogen Generation from Aluminum-Water Reactions	31
1. Introduction.....	31
2. Background.....	31
3. Experimental setup.....	33

4. Results	35
5. Discussion	40
6. Conclusion	41
References to Chapter III.....	42
Chapter IV. Aluminum-water propellant experiments.....	44
Chapter V. Conceptual study of the light gas gun utilizing aluminum-water propellant.....	47

Chapter I. Dual-stage ignition of boron particle agglomerates

Nomenclature

Symb ol	Term	Value or relation used to determine the constant	Unit
A	Pre-exponential factor for boron oxidation	64.8×10^{-8}	$\text{mol/s} \cdot \text{m} \cdot \text{K} \cdot \text{atm}$
C_B	Solid boron heat capacity	$0.507 + 7.0 \times 10^{-5}(T_p)$	$\text{cal/g} \cdot \text{K}$
C_{B₂O₃}	Liquid boron oxide heat capacity	0.438	$\text{cal/g} \cdot \text{K}$
D	Diffusivity of O ₂ in N ₂	0.2	cm^2/s
D_K	Knudsen diffusivity	-	cm^2/s
D_m	Molecular diffusivity	-	cm^2/s
d	Thickness of each layer	-	cm
E_a/R̄	Activation temperature for boron oxidation	22600	K
ΔH_{vap}	Heat of vaporization of liquid B ₂ O ₃	90000	cal/mol
h	Agglomerate-gas heat transfer coefficient	$\frac{(0.347 \times 10^{-6}) \cdot \text{Nu} \cdot T_o^{0.8}}{r_a}$	$\text{cal/cm}^2 \cdot \text{s} \cdot \text{K}$
I	Relative intensity of light	-	Arbitrary unit
i	Index of the current layer	-	-
k	Mass transfer coefficient of B ₂ O ₃ vapor in N ₂	$\frac{(1.18 \times 10^{-7}) \sqrt{T_p} (\text{Nu})}{r_p + X}$	$\text{mol/cm}^2 \cdot \text{atm} \cdot \text{s}$
M_B	Boron molar weight	10.82	g/mol
M_{B₂O₃}	Boron oxide molar weight	69.64	g/mol
Nu	Nusselt number	2.0	-
n_i	Number of boron particles in the <i>i</i> th layer	-	-
P_i	Concentration of O ₂ in the <i>i</i> th layer	-	atm
P_{B₂O₃}^s	Boron oxide vapor pressure	$1.51 \times 10^8 \text{Exp}(-\frac{44000}{T_a})$	atm
Q_R	Heat released by boron oxidation	146000	cal/mol
r_a	Agglomerate radius	-	cm
r_{p,i}	Boron particle radius in the <i>i</i> th layer	-	cm
T_a	Agglomerate temperature	-	K
V_a	Agglomerate volume	-	cm^3

X_i	Thickness of B_2O_3 film in the i^{th} layer	-	cm
α	Evaporation coefficient of liquid B_2O_3	0.04	-
$\beta_{B_2O_3/B}$	Stoichiometric ratio of B_2O_3 to B	0.5	-
$\beta_{O_2/B}$	Stoichiometric ratio of O_2 to B	0.75	-
σ	Stefan-Boltzmann constant	1.354×10^{-12}	$\text{cal}/\text{cm}^2 \cdot \text{s} \cdot \text{K}^4$
ϵ	Agglomerate emissivity	0.8	-
κ	Henry's constant converting partial pressure to concentration O_2	$39.21 \times 10^{-6} \left[-1700 \left(\frac{1}{T_a} - \frac{1}{311} \right) \right]$	$\text{mol}/\text{cm}^3 \cdot \text{atm}$
λ	Wavelength	-	nm
ν	Hertz-Knudsen impingement factor	$5.3/\sqrt{T_a}$	$\text{mol}/\text{cm}^2 \cdot \text{atm} \cdot \text{s}$
$\rho_{B_2O_3}$	Density of solid boron	1.85	g/cm^3
ρ_B	Density of liquid B_2O_3	2.33	g/cm^3

The numerical values of the constants and correlations are adapted from King's model of individual boron particle ignition [5] and [6].

1. Introduction

Elemental boron is an attractive fuel for air-breathing propulsion applications since it has the highest volumetric heat production among all elements in reaction with oxygen, and the third highest heat production potential on a mass basis (after hydrogen and beryllium). Elemental boron powder can be utilized for propulsion in the form of slurries in hydrocarbon fuels [1], in fuel-rich solid propellant formulations [2], or fed directly into the combustion chamber from a compacted powder bed [3]. Agglomeration of the initially micron-sized (crystalline boron) or submicron-sized (amorphous boron) particles inevitably occurs in all of the propulsion applications mentioned above. Porous particle agglomerates in the size range from tens to hundreds of microns are formed as liquid hydrocarbon fuel is evaporated from the droplets in the case of fuel slurries. As particles cluster on the burning surface of a fuel-rich solid propellant, the agglomeration of boron is very pronounced due to the low melting point of the boron oxide glass and its high surface tension and viscosity [4]. The ignition behavior of such particle agglomerates, consisting of hundreds or even thousands of densely packed particles and thus having a large internal reactive surface area, differs considerably from the ignition mechanism of a single micron-size boron particle or a low density particulate suspension. In spite of the obvious practical importance of boron agglomerates, the bulk of experimental and theoretical research literature is dedicated to investigation of ignition and combustion of a single boron particle or low density dust clouds [5,6,7]. Only two prior studies have attempted experimental investigation of the ignition process of boron particle agglomerates. The first study by Shevchuck *et al.* [8] examined ignition of boron particle agglomerates suspended on a tungsten wire in a flow of dry air heated by an electrical furnace up to 1100 K. They found that agglomerates with sizes from 2 to 5 mm comprised of powders of amorphous and crystalline boron can be ignited at temperatures as low as 800 K, in contrast to the much higher temperatures, around 1900 K, that are characteristic for ignition of individual boron particles [9]. This dramatic reduction in ignition temperature did not, however, result in transition to full-fledged boron combustion as expected after a short period of rapid temperature rise; the agglomerates quenched and the degree of boron oxidation was low.

The second study by Holl *et al.* [10] investigated ignition and combustion of boron slurry agglomerates ($r_a = 0.088\text{-}0.4$ mm) supported by a quartz wire in the post-flame gases of a flat-flame burner in the higher temperature range between 1690 and 1950 K. By studying agglomerate images from high speed camera recordings and surface

morphology of the agglomerates quenched at different stages of ignition and combustion, the authors qualitatively identified a multistage ignition and combustion process consisting of the following sequence: 1) heat-up of a porous agglomerate with particles covered by a solid oxide, 2) melting of the oxide to form a liquid coating around each particle with a decrease in the overall agglomerate porosity 3) gasification of the oxide layer that starts around 1900 K leaving an open, porous structure of reacting boron particles 4) melting of the boron (melting point 2450 K) and transformation of the agglomerate to a molten drop consumed by combustion in the external diffusion regime. The authors emphasized observation of the two-stage ignition phenomenon that occurs consecutively. The first stage (the same as observed by Shevchuk *et al.*) occurs at relatively low temperatures under progressively increasing thickness of the oxide layer enveloping individual particles. The second stage follows the first after the agglomerate attains higher temperature that leads to evaporation and removal of the oxide from at least part of the agglomerate surface, thus creating conditions for self-sustained combustion. While the proposed scheme appears plausible, it can be considered only as a hypothesis since the authors neither studied nor explained critical parameters leading to the second stage ignition or quenching, nor performed any *in-situ* measurements of the agglomerate temperature during the ignition process.

The experimental investigation of the ignition characteristics of boron agglomerates reported here used 2-3 mm agglomerates prepared by drying boron/water slurry droplets. The prepared dry agglomerates of a known size, mass, and porosity were then rapidly introduced into a flow of high temperature oxidizing gases obtained by a combination of hydrogen combustion and electrical heating in the case of wet flows ($O_2/H_2O/N_2$) or pure electrical heating for dry flows (O_2/N_2). This technique permitted independently varying the flow temperature and oxygen concentration such that the critical gas composition and temperature for ignition could be determined. By identifying the critical ignition conditions for each stage and monitoring the agglomerate luminosity, spectra, and temperature during the ignition process, the current work has further clarified the physical mechanisms leading to the two-stage boron agglomerate ignition phenomenon. A simple numerical model of the agglomerate ignition process that takes into account oxygen diffusion and the concentration gradient inside the agglomerate is developed in order to interpret the experimental results. The model considers the decrease of oxygen diffusion towards the agglomerate's internal reaction zone due to the buildup of boron oxide that reduces the cross section of the pore channels or blocks the pores completely. The model accurately captures the behavior of the agglomerate two-stage ignition process or quenching, and qualitatively predicts the experimentally observed dependence of the ignition behavior on the agglomerate and flow parameters.

2. Experimental details

2.1 Boron powders

Two different allotropic forms of boron were used in the present experiments: amorphous and crystalline boron powders. Both powders are available commercially from Alpha Aesar. The particle size distributions in the powders were obtained with a Malvern Inc. laser light diffraction instrument (Mastersizer 2000) and are shown in Fig. 1 with other parameters summarized in Table 1 below.

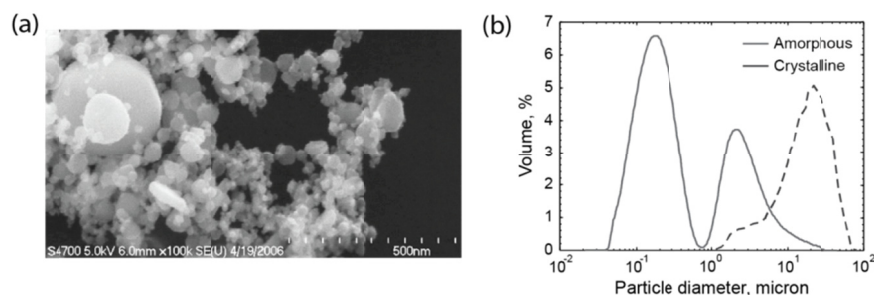


Figure 1 Scanning Electron Microphotograph of the amorphous boron powder (a) and volumetric particle size distribution in amorphous and crystalline boron powders (b).

Table 1 Characteristics of boron powders.

Boron powder	Purity, % (metal basis)	Particle shape	Specific surface area, m ² /g	Particle radius, r_p , μm
Crystalline	98.0	irregular	0.54	3.55
Amorphous	99.0	spherical	26.0	0.105

2.2 Agglomerate preparation

Boron powder agglomerates were prepared by drying 2.5-3 mm droplets of well-stirred boron powder suspensions in water. Each slurry droplet was positioned on a loop of 100 micron tungsten wire and dried in an oven at about 90 °C for about 24 hours (see Fig. 2).

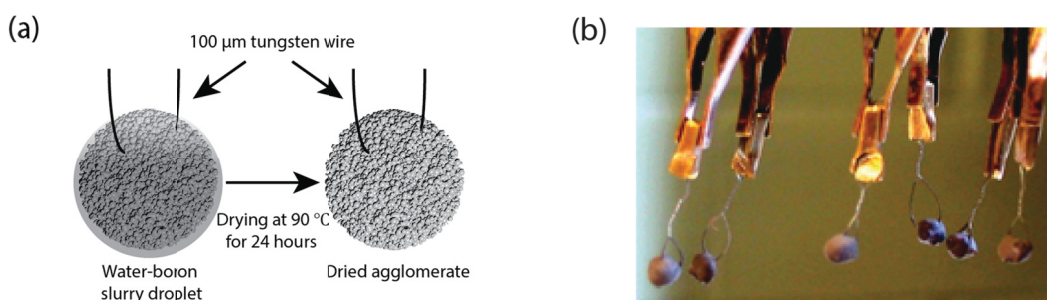


Figure 2 (a) Schematics of the boron agglomerate preparation and (b) photo of the dry boron agglomerate before experiment.

The suspensions of amorphous boron in water were sufficiently viscous and stable to form spherical droplets. One percent of water gelling agent (Polyacrylamide) was added to suspensions of crystalline boron in water to increase viscosity and prevent particle sedimentation. Each slurry droplet was weighed individually with precision electronic balances (accuracy ± 0.1 mg) three times: in the wet state, after drying, and after exposure to the high-temperature flow. Measurements of the slurry droplet size under microscope before and after drying did not register a noticeable change in diameter. Thus, the density of the dry agglomerate can be readily calculated using mass measurements and the densities of boron and water. These measurements have shown good correlation with agglomerate density calculated from the composition of the initial suspension as well as with the approximate density calculations from agglomerate weight and diameter. Calculated densities of the agglomerates were in the range 0.75-0.82 g/cm³ with standard deviation below 10% in a series of 7 to 12 agglomerates typically used for each experimental point.

2.3 Flow and heating

The principle schematics of the experimental setup used in the current work to study ignition of individual boron agglomerates suspended in the high-temperature oxidizing flow is shown in Fig. 3.

For experiments with wet flows, the flow of a gaseous blend of water vapor, oxygen, and nitrogen in the temperature range 700-1100 K was generated using a combination of electrical and combustion heating. A small hydrogen diffusion flame was maintained at the entrance of the first electrical tube furnace as shown in cutaway box in Fig. 3. The total flow rate of gas through the furnace was about 180 cc/s. The flow of hydrogen and the total

flow rate were kept constant, maintaining a stable concentration of water vapor in the flow of around 20%. The oxygen and nitrogen content in the flow was varied from a pure oxygen-water vapor mix (80% O₂/20% H₂O) to a pure nitrogen-water vapor mix (80% N₂/20% H₂O). For dry flows, two similar tube furnaces were connected consequently permitting to maintain the same level of temperature as for wet flows. The flow rate of gases was measured by factory calibrated digital flow meters with 2% accuracy. The flow temperature at the exit of the ceramic nozzle (exit diameter about 18 mm) was monitored by a thermocouple with ± 5 K accuracy. The agglomerate to be tested was manually introduced into the middle of the flow using a sliding post on an optical bench. An end switch closed by the post at the moment of insertion triggered the computer data acquisition for optical diagnostics.

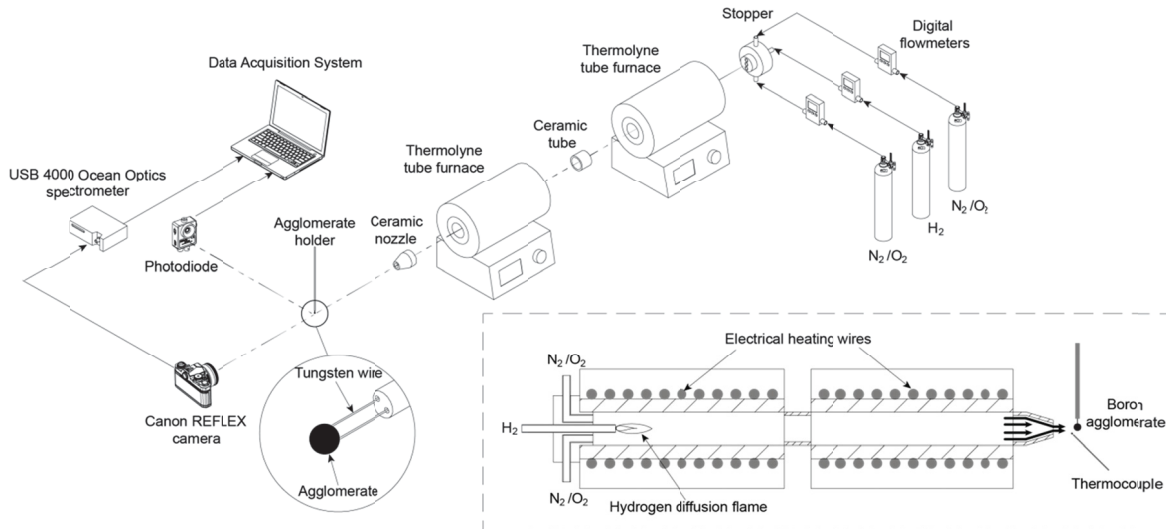


Figure 3 Schematics of the experimental set-up

2.4 Optical diagnostics

Optical diagnostics for the agglomerate ignition process consisted of a photodiode, a miniature fiber optic spectrometer (USB 4000, Ocean Optics) and a video camera. The photodiode, equipped with a single lens focusing system, iris aperture and an amplifier, registered light emitted by the agglomerate in the spectral range 0.4–2.0 μm . The light for the spectral analysis was first collected by a conventional SLR camera with macro T-rings and transmitted to the spectrometer by a 100 micron fiber positioned in the center of the camera's imaging plane (see details in [11]). Because the field of view of the spectrometer was less than 1 mm and smaller than the agglomerate diameter, collection of the background radiation from the furnace and laboratory lights was negligible. The spectrometer permitted acquisition of spectra in the $\lambda = 350\text{--}1100$ nm wavelength range with a spectral resolution of about 2.0 nm. It was set to collect 20 spectra per second with integration time ranging from 20 to 40 ms. Before each series of experiments, the spectrometer was intensity calibrated with a NIST-traceable Ocean Optics LS-1-CAL tungsten halogen calibration lamp. The agglomerate surface temperature was obtained by a polychromatic fitting procedure of the continuum spectra to Planck's law (details in [11]). As illustrated in Fig. 4a, an excellent fit to Planck's law is observed for the spectra emitted during the agglomerate ignition period. The fully developed boron combustion spectra, on the other hand, demonstrated considerable deviation from the "grey" body Planck's law (Fig. 4b) due to an intense set of BO₂ molecular bands covering large parts of the visible spectra. The deviation from the gray spectra for burning agglomerates might also be the result of superposition of the additional spectra emitted by a condensing boron oxide zone enveloping the agglomerate during the combustion stage and having a different temperature than the agglomerate surface, and also by spectrally selective scattering of radiation by submicron boron oxide droplets. Thus, the accuracy of the temperature measurements from the

combustion spectra is estimated to be about ± 250 K, as opposed to an order of magnitude higher accuracy of ± 25 K estimated for the spectral temperature measurements during the ignition stage.

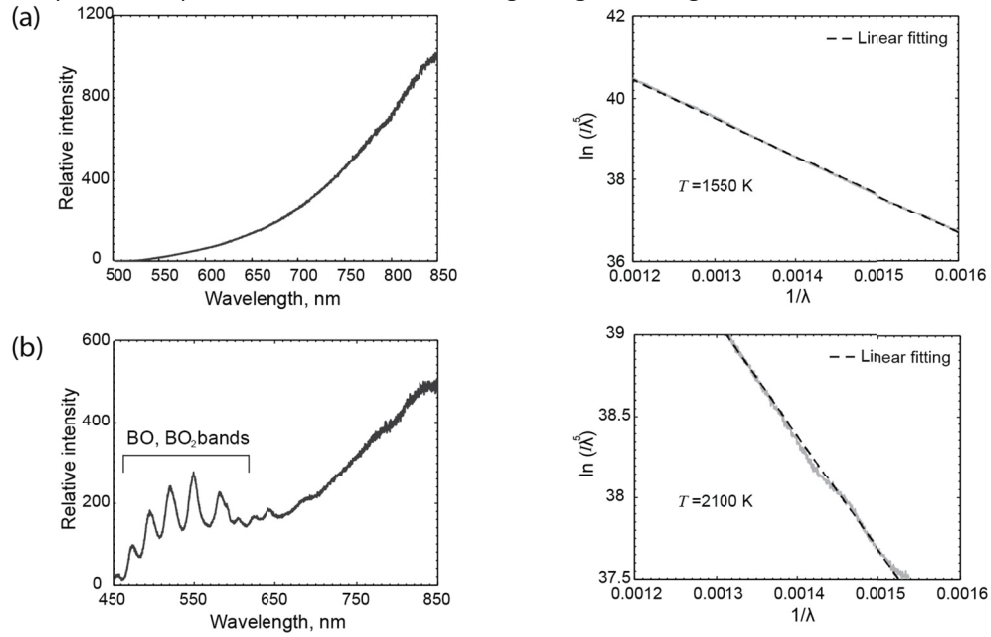


Figure 4 Spectral intensity and fitting to the Planck's law of the agglomerate (a) ignition and (b) combustion spectra

3. Experimental

3.1 Two-stage agglomerate ignition phenomenon

The two-stage ignition process of the boron agglomerates was evident from light intensity traces registered by the photodiode, the dynamic spectral measurements of the agglomerate surface temperature, and the video recording of the ignition process. As can be seen from the photodiode traces and video frames shown in Figs. 5 and 6, the sharp increase in agglomerate luminosity was observed after introduction of the agglomerate into an oxidizing flow having a temperature above some critical value. At low oxygen concentrations, however, the agglomerate rapidly quenched after the first ignition stage.

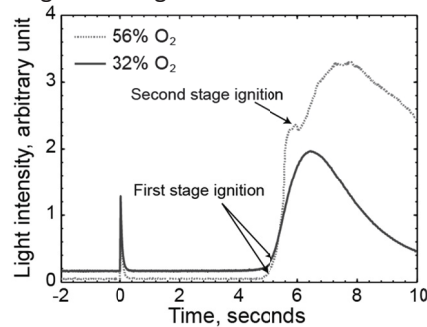


Figure 5 Agglomerate luminosity history registered by the photodiode during the first and the second stage ignition

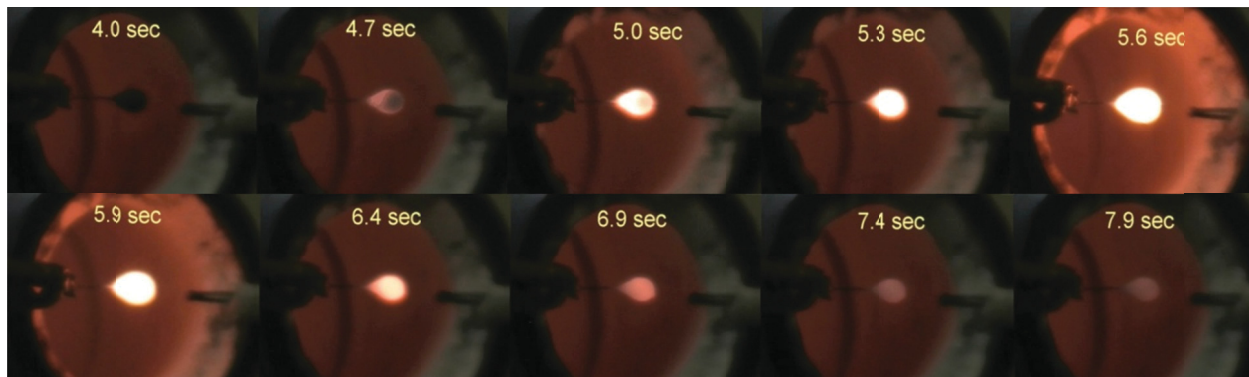


Figure 6 Video frames of the agglomerate first stage ignition that is followed by agglomerate quenching

The quenched agglomerate became very hard, monolithic, and difficult to crush. The evaluation of the quenched agglomerate surface under a microscope showed that it was covered with a layer of transparent boron oxide film. The boron oxide was also clearly visible inside the remains of the crushed agglomerate. All quenched agglomerates demonstrated a considerable mass increase (see below).

If the oxygen concentration in the flow was at or above some critical value, a second ignition stage that followed the first ignition stage was observed (Figs. 5, 7). As can be seen from Fig. 5, the agglomerate luminosity reached a short plateau after the first stage ignition and then rapidly started to rise again, leading to a fully developed combustion stage wherein the agglomerate was completely consumed. At oxygen concentrations above, but close to, critical a fairly long combustion stage was often observed while the agglomerate was still attached to the supporting tungsten wire. At oxygen concentrations exceeding critical, the agglomerate usually dropped off supporting wire soon after the second stage ignition.

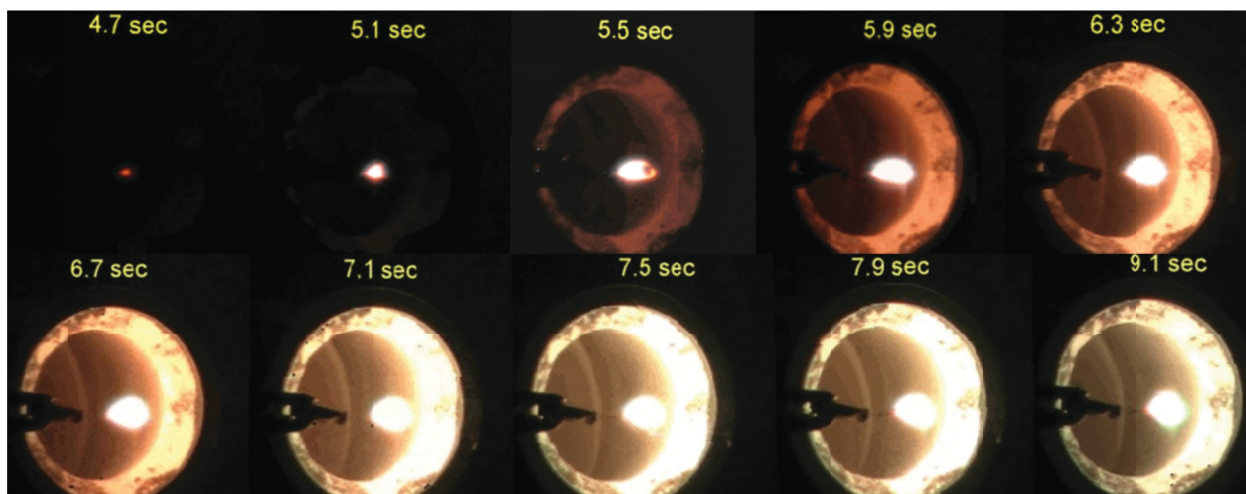


Figure 7 Video frames of the agglomerate first (5.1–5.5 s) and the second (6.3–6.7 s) ignition stages followed by fully fledged combustion.

It is interesting to note that even at oxygen concentrations well above critical, the onset of the second ignition stage could still be clearly identified. In this case, however, it was manifested not by a plateau in agglomerate luminosity and temperature but rather by a sharp change in their rate of rise.

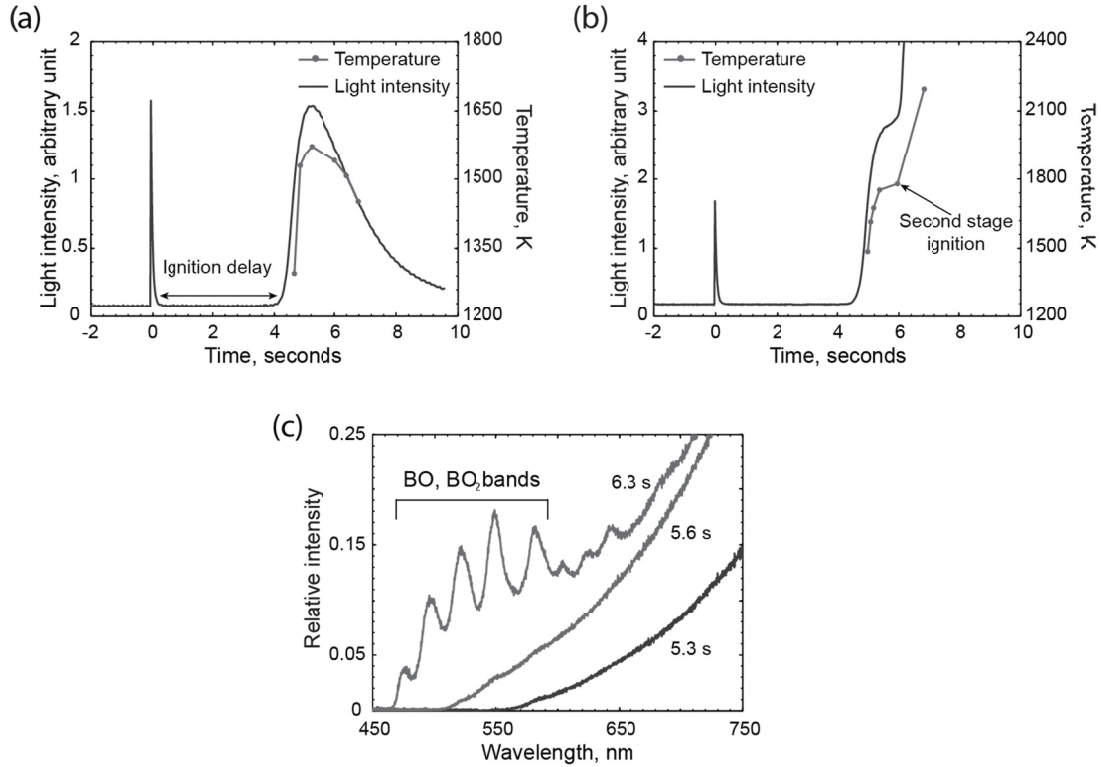


Figure 8 Time history of the agglomerate surface temperature during (a) the first stage ignition and quenching and (b) the second stage ignition, and (c) agglomerate spectra at different moments of the dual-stage ignition process.

3.2 Boron agglomerates ignition characteristics in wet flows

In order to obtain oxidizing flows with the same oxygen concentration, but at different temperatures, the electrical furnace was turned off after the flow reached a stable temperature around 1050 K. The following slow decline in the flow temperature allowed performing ignition experiments at fairly stable conditions. The measured dependence of the first stage ignition delay time (i.e., the time delay between insertion of agglomerate into the flow and the appearance of luminosity) and the peak temperature attained by the agglomerates before quenching at different flow temperatures are plotted in Fig. 9 for the crystalline boron agglomerates.

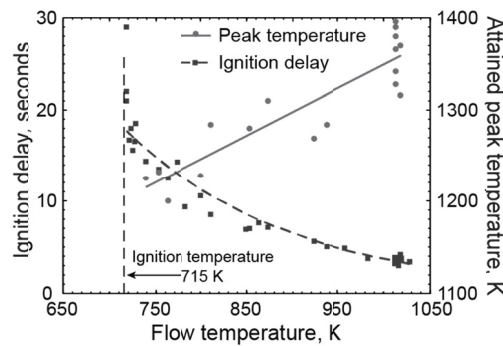


Figure 9 Delay times and maximum attained temperature before quenching of the first ignition stage for the crystalline boron agglomerates.

As can be seen from Fig. 9, the ignition temperature for the crystalline boron agglomerates was found to be about 715 K and is close to the melting/softening point of glassy boron oxide of about 720 K [4]. The ignition delay time increased exponentially as the flow temperature approached this value, in agreement with the predictions of

the classical theory of thermal explosion [13]. The effect of the flow temperature on peak temperature attained by the agglomerate after ignition was rather weak. It increased by less than 150 K with an increase in flow temperature of about 300 K. It was also found that the first stage ignition temperature was practically independent of oxygen concentration in the range between 21% and 80% oxygen in the flow.

Contrary to expectations and in contradiction to the experimental results obtained in [8], it was found that the first stage ignition temperature for the amorphous boron agglomerates having the same density and same overall size as the crystalline boron agglomerates was about one hundred degrees higher: 828 K, compared to 715 K for crystalline boron. This indicates that not all the inner surface of the amorphous boron agglomerate (as seen from Table 1, almost 50 times larger than for crystalline boron) was accessible to oxygen during the ignition process. The reason for such behavior is discussed in the section below.

In contrast to the first stage ignition temperature that was not affected by the oxygen concentration, the peak temperature attained by the agglomerate after ignition increased sharply with the increase in oxygen content in the flow (Fig 10). Experimental data also show that the time elapsed from the moment of ignition to the occurrence of the peak temperature also decreased steadily with an increase in oxygen concentration for both crystalline and amorphous particle agglomerates.

As shown in Fig. 10(a), amorphous boron agglomerates start to undergo the second ignition stage at oxygen concentrations close to 44% O₂. The plateau temperature that the agglomerate reached at critical oxygen concentration before the second ignition stage was, on average, about 1690 K. The change in agglomerate mass shows large scattering at critical oxygen concentration with some agglomerates demonstrating considerable weight loss. The agglomerate weight loss indicates a rapidly increased rate of evaporation of the liquid boron oxide B₂O₃. Quenched amorphous boron agglomerates exhibited a steady increase in mass gain up to 45% before undergoing the second stage ignition at an oxygen concentration of about 44%.

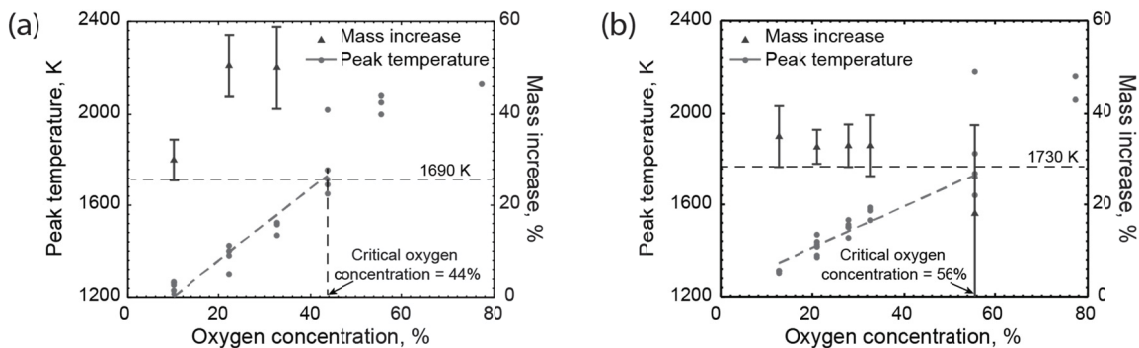


Figure 10 Maximum attained agglomerate temperature and agglomerate mass gain as a function of oxygen concentration in the wet flows for (a) amorphous and (b) crystalline boron agglomerates

The maximum mass gain for the crystalline boron agglomerates after the first ignition stage followed by quenching was at about 35%, as shown in Fig. 10(b). It was practically independent of oxygen concentration and about 10% lower than for amorphous boron. This mass gain would translate to about 11% of the oxidized boron if one neglects evaporation of the boron oxide. The average maximum temperature of 1730 K reached by crystalline agglomerates before the second stage ignition was practically the same as for amorphous boron agglomerates within the estimated accuracy of the temperature measurements.

3.3 Boron agglomerate ignition characteristics in dry flows

Dry oxidizing gas flows were produced by pure electrical heating of the corresponding O₂-N₂ gas mixtures flowing through two consecutively connected tube furnaces (see Fig. 3). The qualitative ignition characteristics of boron agglomerates in dry flows were essentially the same as in wet flows. The two-stage ignition phenomenon

was also observed. As in the wet flows, agglomerates quenched if the oxygen concentration in the flow was below some critical value or underwent the second stage ignition followed by combustion at higher oxygen concentrations. The values of the first stage ignition temperatures and the critical oxygen concentrations needed for the second stage ignition in dry flows were, however, noticeably higher, demonstrating the positive effect of boron oxide gasification by water vapors on the boron ignition process. The ignition characteristics of boron agglomerates in wet and dry flows are compared in Table 2 below. Though the presence of water vapors in the flow did not change the two-stage agglomerate ignition process qualitatively, water vapor noticeably decreased the first stage ignition temperature and the critical oxygen concentration for the second stage ignition both for crystalline and amorphous boron agglomerates, as shown in Table 2.

Table 2 Comparison of agglomerates ignition characteristics in wet and dry flows

F low	Boron	1st ignition temperature, K	2nd ignition critical O₂ concentration, %	2nd ignition temperature, K
2 0 % H ₂ O	Crystalline	715	56	1730
	Amorphous	828	44	1690
Dry	Crystalline	896	70	1890
	Amorphous	958	55	1860

4. Physical model of boron agglomerate ignition

4.1 Model Objectives

As can be seen from the experimental results presented in Section 3, the most prominent feature of the boron agglomerate ignition process that separates it from ignition of a single particle is the observed two-stage ignition phenomenon. Unlike for a single particle, wherein ignition, once started, leads to particle combustion in the diffusion regime [5], the thermal explosion that occurs within the boron agglomerate at relatively low temperatures does not always result in a transition to self-sustained combustion. If the oxygen concentration in the flow is below some critical value, ignition is followed by agglomerate quenching and the degree of boron oxidation is low. At higher oxygen concentrations, thermal ignition of the agglomerate results in a transition to self-sustained combustion via the second ignition event, as manifested by a distinctive kink in the rate of temperature increase (see Fig. 8(b)) and, at oxygen concentrations close to critical, is observed after the temperature history briefly takes on a plateau value. Thus, the main objective of the theoretical effort described below is to identify the key physical mechanisms responsible for the agglomerate quenching and the dual ignition phenomenon while simplifying other aspects of the complex agglomerate ignition process as much as possible.

4.2 Model assumptions

Ignition of a single boron particle, as described by the classical model of King [5,6], is governed by the interaction between boron oxidation through the protective layer of the boron oxide liquid film and film removal due to evaporation and gasification by water vapor in wet flows. Ignition occurs at the temperature at which the rate of film evaporation and gasification [14] exceeds its rate of growth, leading to a rapid decrease in the film thickness, eventually exposing the bare boron surface to the flowing oxygen. Due to the low diffusivity of oxygen

through boron oxide in comparison to gas, the oxygen concentration at the external surface of the oxide film that envelopes the particle during the entire ignition process is practically equal to the oxygen concentration in the free flow. Thus, the gaseous diffusion of oxygen can be neglected until the boron surface becomes practically free of the oxide film. Unlike a single isolated particle, boron particles at different distances from the inside surface of the agglomerate are exposed during the ignition process to constantly changing oxygen concentrations that are considerably lower than that in the free flow due to oxygen consumption in the outer agglomerated layers and the higher diffusion resistance of the porous media in comparison to gases. In the course of ignition, the oxide film around each particle grows, the cross section of the agglomerate pores decreases, leading to a proportional decrease in the oxygen diffusivity inside the agglomerate.

The most important simplifications assumed by the model can be summarized as follows:

- The agglomerate and all constituent particles are of spherical shape. All particles have equal size.
- The agglomerate is assumed to be isothermal, i.e., any temperature gradient inside the agglomerate is neglected.
- The heat exchange with the environment via convection and radiation takes place through the external surface of the agglomerate.
- The boron oxide is evaporated in the kinetic regime, i.e., diffusion resistance to oxide vapors inside the agglomerate is neglected. Consequently, outflowing boron oxide vapors have no effect on the oxygen diffusion inside the agglomerate.
- The model considers ignition only in dry flows and thus neglects gasification of the boron oxide by water vapor.

4.3 Layered agglomerate ignition model and its governing equations

The agglomerate temperature, the mass of each boron particle inside the agglomerate, and the thickness of the oxide film covering the particles are the time-dependent parameters. The reaction rate of a boron particle covered by a film of liquid boron oxide depends on the thickness of the film, temperature, and the current oxygen concentration to which the particle is exposed. Due to the constantly changing gradient of oxygen concentration inside the agglomerate, the reaction rate of each particle, and therefore its mass and the mass of the boron oxide, are also spatially dependent parameters.

In our model, we approximate the gradient of oxygen concentration inside the agglomerate by steps. In this approximation the agglomerate is divided, as shown in Fig. 11(b), into N equidistant concentric layers (shells). The oxygen concentration inside each layer is considered to be uniform and varies only with time. Thus all particles within each layer have an equal radius and the equal thickness of the oxide film. An oxygen concentration profile inside the agglomerate at each time step can be obtained by solving the diffusion equation in reacting media with the diffusion resistance in each layer to be proportional to a time-dependent pore diameter. The pore diameter in each layer can be calculated by tracking the change of the external particle radius which is the sum of the boron particle radius and the thickness of the oxide film.

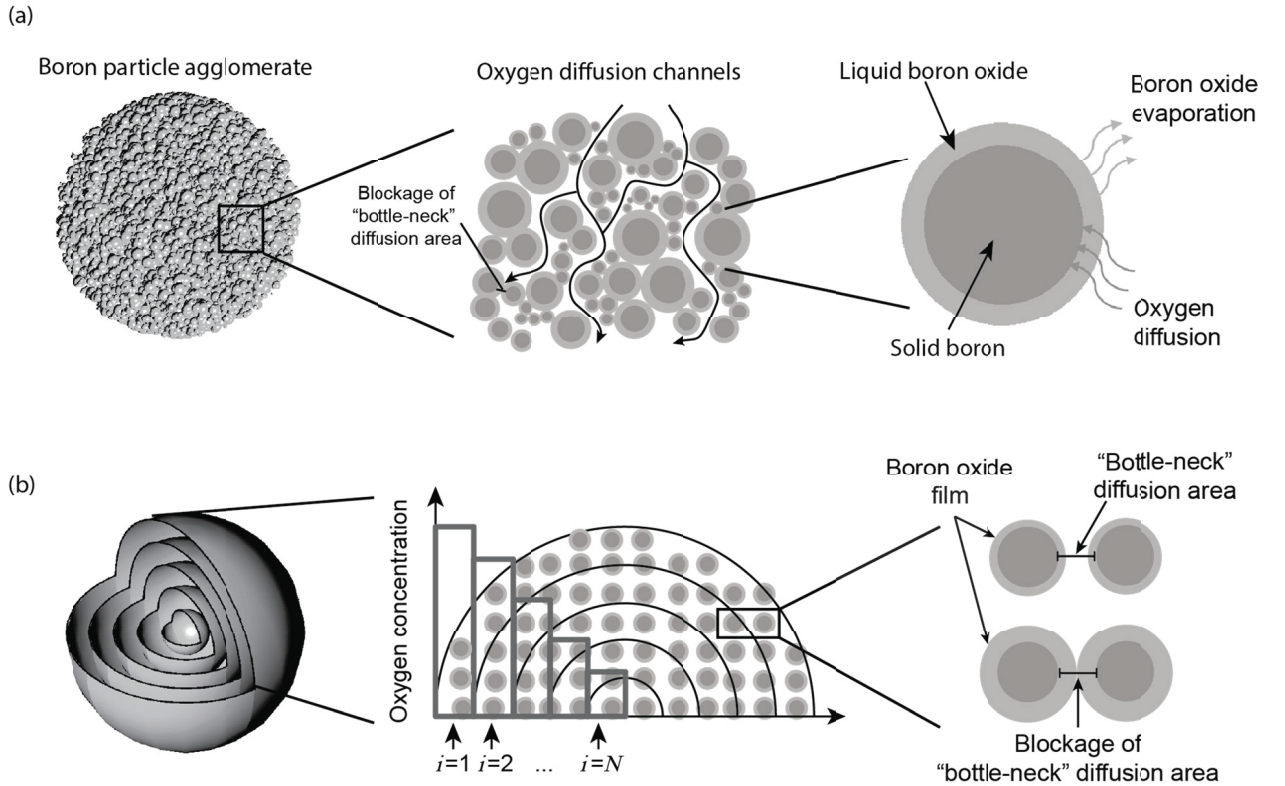


Figure 11 (a) Illustration of the realistic boron particle agglomerate, oxygen diffusion channels, and individual reacting boron particle; (b) illustration of the simplified model of the boron particle agglomerate and the concept of "bottle-neck" diffusion area

Based on the above stated assumptions and limitations, the heat balance equation can be written as follows (where i is the index of the current layer, n_i is the number of particles in the i^{th} layer, and N is the total number of layers):

$$Q_R \sum_i^N n_i \cdot R_{B,i} - (\Delta H_{\text{vap}}) \sum_i^N n_i \cdot R_{E,i} = -4\pi r_a^2 [h(T_p - T_0) + \sigma \cdot \epsilon \cdot (T_a^4 - T_0^4)] + \quad (1)$$

The left hand side of Eq. (1) takes into account the change in mass of the boron and boron oxide within the agglomerate by summarizing the heat capacities of agglomerate layers. The first term on the right hand side represents the rate of heat transfer via convection and radiation through the external surface of the agglomerate. The second term is the rate of heat generation by the reaction of boron with oxygen. The last term describes the rate of heat loss caused by evaporation of liquid boron oxide.

The mass balance equation for the boron oxide in the i^{th} layer can be written as:

$$\frac{dx_i}{dt} (4\pi r_{p,i}^2 \rho_{B_2O_3}) = (\beta_{B_2O_3/B} \cdot R_{B,i} - R_{E,i}) M_{B_2O_3} \quad (2)$$

and the mass balance equation for boron in the i^{th} layer as:

$$\frac{dr_{p,i}}{dt} (4\pi r_{p,i}^2 \rho_B) = -R_{B,i} \cdot M_B \quad (3)$$

For each boron particle inside the agglomerate, the model adapts the same boron oxidation (4) and boron oxide evaporation (5) laws as formulated by King for a single particle ignition model [5]:

$$R_B = \frac{A \cdot r_p^2 \cdot P \cdot T_p \cdot \exp\left(\frac{-E_a}{R \cdot T_a}\right)}{X} \quad (4)$$

$$R_E = \frac{4\pi(r_p + X)^2 \alpha v P_{B_2O_3}^0}{1 + \alpha v / k} \quad (5)$$

As illustrated in Fig. 11(a), the reaction is limited by the oxygen diffusion rate through the liquid boron oxide film and is inversely proportional to its thickness (4). The rate of the boron oxide evaporation in King's formulation considers both the kinetic and the diffusion resistances. However, since in the current model the concentration of boron oxide vapor inside the agglomerate is assumed to be equal to that of the free stream, the evaporation rate is controlled by kinetics.

The oxygen concentration profile at each time step of the agglomerate ignition process can be found by solving a steady-state oxygen diffusion equation in each layer:

$$D \left(\frac{\partial^2 P}{\partial r^2} + \frac{1}{r} \cdot \frac{\partial P}{\partial r} \right) - K \cdot P = 0 \quad (6)$$

$$\text{where } K = \frac{N_p \cdot \beta \cdot A \cdot r_p^2 \cdot T_a \cdot \exp\left(\frac{-E_a}{R \cdot T_a}\right)}{V_a \cdot \kappa \cdot X}$$

The analytical solution for equation (6) is the zero-order modified Bessel function:

$$P(r) = C_1 I_0 \left(\sqrt{\frac{K}{D}} r \right) + C_2 J_0 \left(\sqrt{\frac{K}{D}} r \right) \quad (7)$$

where C_2 is equal to zero since P_N must be finite. Using an approximation of I_0 by a second order series, Eq. (7) can be simplified as follows:

$$P_{(r)} = C_1 \left(1 + \frac{K}{4D} r^2\right) \quad (8)$$

The unknown coefficient C_1 in i^{th} layer can be found from the partial pressure of oxygen in the previous $i-1$ layer and the expression for the oxygen partial pressure in the i^{th} layer can be written as follows:

$$P_i = \frac{4 \cdot D \cdot P_{i-1}}{4 \cdot D + K[r_a - (i-2) \cdot d]^2} \times \left\{1 + \frac{K}{4D} [r_a - (i-1) \cdot d]^2\right\} \quad (9)$$

Here $d = r_a/N$ is the thickness of each layer.

As the oxygen concentration in the external layer ($i = 1, r = r_a$) is always close to that in the free flow, the oxygen concentration profile inside the agglomerate can be computed recursively from the top layer to the last bottom layer at each time step.

The delivery of oxygen inside agglomerate by the gas diffusion through the pores is interrupted when the growing layer of the boron oxide blocks the pore channel cross section at some ‘bottle-neck’ location inside the agglomerate as schematically illustrated in Fig. 11(c). Even for an ideal mono-disperse spherical powder, the pore cross section in high porosity agglomerates varies due to density fluctuations and the formation of branch-like structures [15]. Both the crystalline and amorphous boron powders used in the present experiments have wide particle size distributions, as shown in Fig 1, that will result in an even larger distribution of pore size. Thus defining the bottle-neck distance is somewhat arbitrary and has to be calibrated by comparing model predictions to qualitative experimental results. The model predicts that if the bottle-neck distance is chosen to be above 20% of the average pore diameter, the agglomerate consisting of spherical monosize particles will not quench under any circumstances after undergoing the first stage ignition. On the other hand, if the bottle-neck cross section is below 6% of the average pore diameter, the agglomerate always quenches after the first stage ignition without undergoing a transition to the second stage combustion. Thus for the calculation shown below we have considered bottle-neck cross section to be about 10% of the average pore diameter.

When in the process of calculations the growth of the boron oxide film exceeds the chosen critical width of the bottle-neck area in the i^{th} layer, the channel is plugged and both oxygen diffusion and boron oxide evaporation are blocked in the layers underneath. The model predicts (see below) that blocked channels may re-open in later times if the thickness of boron oxide decreases below critical width due to intensive evaporation at high temperatures. Hence, the number of ‘active’ layers participating in oxidation is constantly changing and may first decrease and then increase in the course of the ignition process.

4.4 Theoretical results, comparison with the experiment, and discussion

The numerical simulation of the agglomerate reacting in dry oxidizing flow has been performed with the model dividing the agglomerate into 100 equidistant layers. Numerical values for the boron oxidation reaction constants in Eq. (3) and boron oxide evaporation in Eq. (5) were taken from King’s work [5]. The radiation emissivity of the external surface of the agglomerate is assumed to be 0.8 and the heat and mass transfer coefficients inside and outside the agglomerate were considered temperature dependent in accordance to established values in the literature [16]. The calculated time-temperature history of the agglomerate that is rapidly inserted into the oxidizing flows having different temperatures but the same 20% oxygen content is shown in Fig. 12(a). As shown in Fig. 12(a), the model correctly captures the qualitative picture of the agglomerate two-stage ignition process. Below 1150 K the agglomerate undergoes only an inert heating to the flow temperature. At about 1150 K, the thermal explosion within the agglomerate rapidly elevates its temperature to the peak value of about 1500 K, after which the reaction practically stops and the agglomerate begins to cool down to the flow temperature as an inert body. At flow temperatures above 1190 K, after the agglomerate temperature briefly reaches a plateau at about 1600 K, the second ignition stage occurs and is manifested by a very sharp rise in agglomerate temperature and the intensive evaporation of the boron oxide within the agglomerate. The model results also confirm the experimental observations that transition from the first to the second stage ignition can be

induced by the increase of oxygen concentration at a relatively low flow temperature. Thus Fig. 12(b) shows results of the model simulation of the agglomerate ignition process at different oxygen concentrations at flow temperature of 1050 K. The model predicts transition from the first to the second stage ignition at 79% of O_2 , whereas experiments performed in dry flows show transition at approximately 70% of O_2 for crystalline boron agglomerates (see the results in Table 2).

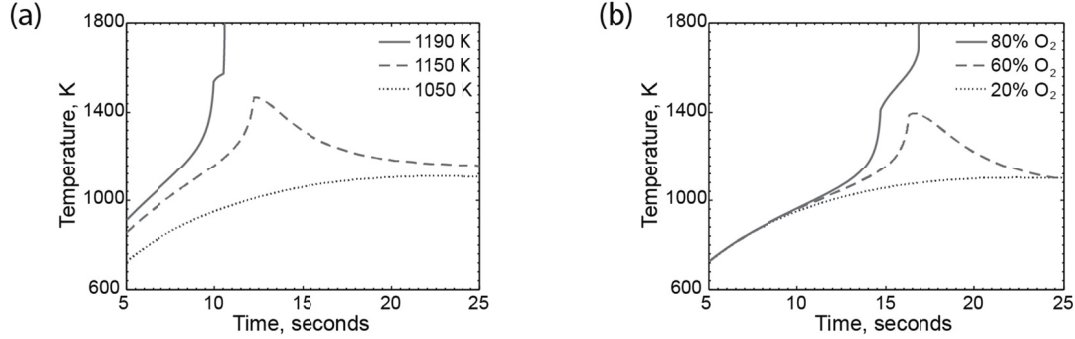


Figure 12 Model results showing time history of agglomerate temperature inserted into dry oxidizing flows with (a) different temperatures and the same 20% oxygen content and (b) with different oxygen concentrations at 1050 K. Agglomerate diameter is 3 mm, boron particle size is 3 μm , initial thickness of the boron oxide film is 0.01 μm , and the agglomerate density is 0.8 g/cm³.

As mentioned before, the difference between ignition of a single particle and agglomerate is that, in the case of the agglomerate, the reaction surface area within the agglomerate is exposed during ignition to a dynamically changing oxygen concentration that depends both on the distance from the agglomerate surface and time, whereas, in the case of a single particle, the concentration of oxygen on the outside surface of the boron oxide layer is constant. At some point, the oxygen access to layers below some location deep within the agglomerate can be completely cut off by the boron oxide film blocking the channel at a bottle-neck location. The complex dynamics of oxygen concentration profiles within the agglomerate during the two stage ignition process is illustrated in Fig. 13.

During inert agglomerate heating (curve 1) the oxygen concentration within the agglomerate, as shown in Fig. 13, is practically the same as in the free flow. The first stage ignition is manifested by a sharp drop in oxygen concentration with radius (curve 2) making reaction effectively localized in layers close to the agglomerate surface. Eventually the reactive surface below some point inside the agglomerate is completely cut off from oxygen by a blockage of the pore channel by the build-up of the boron oxide (curve 3). This leads to a rapid drop in the reaction rate and coincides with a plateau on the temperature curve. The beginning of the plateau is effectively a “tipping point.” If the agglomerate temperature is sufficiently high, the evaporation of the boron oxide eventually removes the oxide pore blockage, permitting once again oxygen delivery deep inside the agglomerate (curve 4). The rapidly increased reaction surface area, in combination with high temperature and the thinner oxide film, leads to exponential temperature increase and fast evaporation of the remaining boron oxide, resulting in transition to self-sustained agglomerate combustion. In the opposite case, when the temperature is not high enough, the pore blockage progresses towards the surface of the agglomerate, shrinking the reaction surface area to just the external agglomerate surface, resulting in quenching.

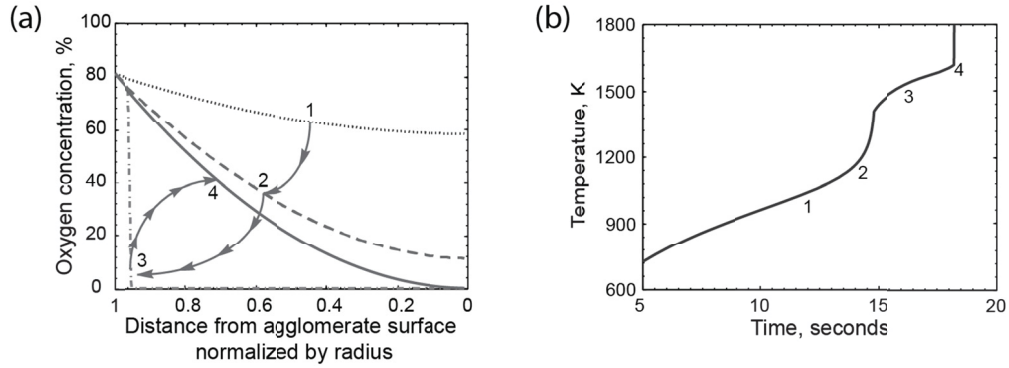


Figure 13 Model results showing (a) concentration profiles inside agglomerate during different stages of the ignition process and (b) the corresponding time history of agglomerate temperature. 1- Inert heating before the first stage ignition, 2-during the first stage ignition, 3-at a temperature plateau tipping point and 4-during the second stage ignition.

The numerical results obtained from the model are also in relatively good quantitative agreement with experimental results obtained for crystalline boron agglomerates in dry oxidizing flows. Thus, as mentioned before, the model predicts a critical oxygen concentration for the second stage ignition of 79% versus the experimental value of 70% and predicts the first ignition temperature of 1050 K in comparison to 900 K measured experimentally. Due to the very large specific surface area of amorphous boron (see Table 1), the model predicts that the first ignition stage temperature for amorphous boron agglomerates should be lower in comparison to crystalline boron agglomerates. As can be seen from Table 2, this prediction contradicts experimental result showing that crystalline boron agglomerates ignite at lower flow temperature than amorphous boron agglomerates. This suggests that the current model based on molecular diffusion in porous media is not applicable to amorphous boron agglomerates. Indeed, as seen from Fig. 1, amorphous boron contains a large number of nano-sized particles, and the second peak of the bimodal particle size distribution in amorphous boron powder is at about 100 nm. The mean path length between molecular collisions at 1000 K is about 230 nm, suggesting that diffusion in pores associated with the nanometric tail in particle size distribution is of the Knudsen type, even at the beginning of the ignition process. The total diffusion resistance of the oxygen delivery inside the agglomerate can be presented as the sum of molecular $1/D_m$ and Knudsen $1/D_k$ diffusion resistances: $1/D = 1/D_m + 1/D_k$ [17]. Because the mean molecular free path is proportional to the gas temperature, the role of slower Knudsen diffusion increases and dominates in later stages of the ignition process for the amorphous boron agglomerate. Thus, the model developed above should be modified in future to include Knudsen diffusion in order to be applicable to amorphous boron agglomerates.

5. Conclusion

Agglomeration of particles, often observed in various propulsion systems utilizing metal fuel, has always been viewed as a purely deleterious phenomenon that increases combustion time of the fuel and frequently leads to a loss in specific impulse. As shown in the current work, this negative effect can be offset, at least partially, by a drastic reduction in the ignition temperature of the agglomerate in comparison to a single particle. Thus, for boron, whose high ignition temperature was always considered detrimental for efficient utilization, the reduction in ignition temperature observed with agglomerates in comparison to single particles can exceed 1000 K.

The ignition of the boron agglomerate is shown both experimentally and theoretically to be a dual stage phenomenon resulting from a complex interplay between boron oxidation, evaporation of the oxide, and diffusion of oxygen towards the large internal agglomerate surface area. Because of the large reactive surface area, the first ignition stage of the agglomerate occurs at relatively low temperatures when evaporation of the boron oxide is practically negligible. The build-up of the boron oxide inside the agglomerate during the first stage ignition process eventually blocks diffusion delivery of oxygen towards the agglomerate internal surface and may result in

agglomerate quenching. However, if the peak temperature reached during the first ignition stage is sufficiently high, the rapid evaporation of the oxide eventually unblocks the internal surface for reaction providing conditions for the second stage ignition. The second ignition stage results in complete evaporation of the oxide from both external and internal surfaces of the agglomerate, resulting in transition to agglomerate combustion controlled by diffusion external to the agglomerate.

References to the Chapter I.

1. P.R. Choudhury. Slurry fuels. *Prog. Energy Combust. Sci.* 18 (1992) 409-427.
2. V.A. Babuk, V.A. Vassiliev and V.V. Sviridov. Propellant Formulation Factors and Metal Agglomeration in Combustion of Aluminized Solid Rocket Propellant. *Combust. Sci. Technol.* 163 (2001) 261–289.
3. S. Goroshin, A.J. Higgins, and M. Kamel. Powdered metals as fuel for hypersonic ramjets. 37th AIAA/ASME/SAE/ASEE Joint Propulsion Conference & Exhibit 2001: Salt Lake City, Utah.
4. G.V. Samsonov, *The Oxide Handbook*, IFI/Plenum, New York, 1982, p. 463
5. M.K. King. Boron Ignition and Combustion in Air-Augmented Rocket Afterburners. *Combust. Sci. Technol.* 5 (1972) 155-164
6. M.K. King, Boron Particle Ignition in Hot Gas Streams. *Combust. Sci. Technol.* 8 (1973) 255-273
7. A.N. Zolotko, L.A. Klyachko, K.M. Kopeika, D.I. Polischuk, V.G. Shevchuk. Critical ignition conditions for boron particles suspended in a gas. *Combust. Explo. Shock Wave* 13 (1977) 31-36
8. V. G. Shevchuk, A.N. Zolotko, and D.I. Polishchuk. Ignition of packed boron particles. *Combust. Explo. Shock Wave* 11 (1975) 189-192
9. A. Maček, and J.M. Semple. Combustion of Boron Particles at Atmospheric Conditions. *Combust. Sci. Technol.* 1 (1969) 181-191
10. J. T. Holl, S. R. Turns, A. S. P. Solomon, and G. M. Faeth. Ignition and Combustion of Boron Slurry Agglomerates. *Combust. Sci. Technol.* 45 (1986) 147-166
11. S. Goroshin, J. Mamen, A. Higgins, T. Bazyn, N. Glumac, H. Krier. Emission spectroscopy of flame fronts in aluminum suspensions. *Proc. Combust. Institute* 31 (2007) 2011–2019
12. M. J. Spalding, H. Krier, R.L. Burton. Boron suboxides measured during ignition and combustion of boron in shocked Ar/F/O₂ and Ar/N₂/O₂ mixtures. *Combust. Flame* 120 (2000) 200–210
13. D. A. Frank-Kamenetskii, *Diffusion and Heat Transfer in Chemical Kinetics*, Plenum, New York, 1969, p. 320–352.
14. G. Mohan, F. A. Williams. Ignition and Combustion of Boron in O₂/Inert Atmospheres. *AIAA Journal* 10 (1972) 776-783
15. K. Vafai, *Handbook of Porous Media*, CRC Press, 2009, p. 928
16. W.M. Haynes, *CRC Handbook of Chemistry and Physics*, 93rd Edition, CRC Press, 2012, p. 2664
17. C. E. Wicks, R.E. Wilson, and G.L. Rorrer, *Fundamentals of Momentum, Heat, and Mass Transfer*, 4th Edition, John Wiley & Sons, 2000, p. 780

Chapter II. Combustion of Boron-Aluminum suspension in products of the hydrocarbon flame

1.1 Introduction

The use of boron in air-augmented combustion either in a hydrocarbon matrix [1] or as purely metal powder fuel ramjet [2] has been considered as a method to boost the energy density of fuels and to provide a safe, thermally insensitive propellant with a long shelf life. The use of catalytic substances has been proposed (fluorine oxidizers, H_2O vapor, etc) [3, 4] as a potential way to increase reaction rates and provide pathways for more energetically favorable combustion. An even simpler way to accelerate the boron reaction is to combine the boron powder with a more reactive constituent (binary mixture of powdered metal fuels). The more energetic component of the fuel raises the temperature of the mixture theoretically allowing for faster boron reactions.

Analogous to the stabilization of the air-fuel mixture produced by a fuel-rich propellant in a ducted rocket, a flow metal powder suspension in air has the ability to sustain a flame on a nozzle. [5]. It has been shown that when mixed with hydrocarbon fuel, the flame front of the aluminum couples with the hydrocarbon front allowing flame stabilization at lower concentrations of metal fuel [6]. This is analogous to boron metal combustion and flame propagation in propellant formulations with metal and hydrocarbon fuel. Hydrocarbon fuel allows presence of hydroxyl groups reacting with BO to form metaboric acid (HOB O) and boron oxide hydride (HBO) which are B_2O_3 oxidation reaction inhibitors at the high temperatures in the flame. It is unknown how the hydrocarbon presence will affect flame propagation in aluminum boron mixtures.

There is also considerable interest to determine the effect of the boron loading and the ability to contribute to the flame propagation in the aluminum-hydrocarbon coupled flame front as demonstrated by Soo et al. [6]. This study is meant to examine laminar flame propagation in suspensions of aluminum-boron powder mixtures in air and in a hydrocarbon flame.

1.2 Boron Mixtures

Boron has a hygroscopic oxide layer which makes dispersion difficult due to its tendency to agglomerate. However, when mixed with aluminum powder in small weight fractions, the powder mixture is capable of laminar dispersion. A 5% (gravimetric) mixture of amorphous boron and 95% aluminum were used to study the flame propagation of the dust suspension in 26% oxygen.

The experiments were performed with a mixture of 15% (gravimetric) amorphous boron and 85% aluminum. The powders were mixed batches of 100g in a laboratory powder mixer. The powders were then dried overnight to remove any excess moisture to minimize agglomeration. The aluminum powder used was Ampal 637 and amorphous Boron. The size-distribution was acquired with the Malvern Mastersizer 2000 and is shown for each individual powder in Figure 1 and Figure 2 and in the 15% boron mixture in Figure 3.

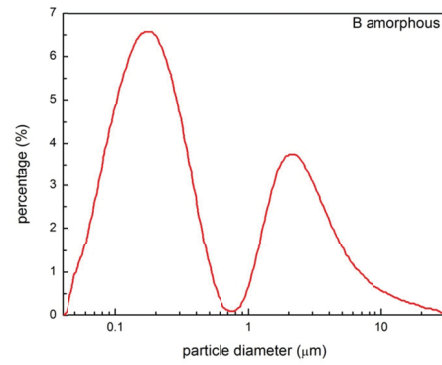
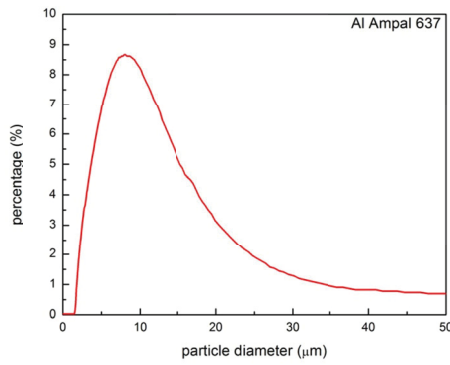


Figure 13. Size distribution of Ampal 637, $d_{32} = 5.6 \mu\text{m}$. Figure 14. Size distribution of amorphous boron, $d_{32} = 0.212 \mu\text{m}$

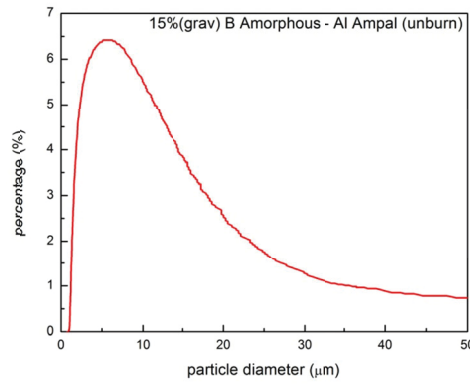


Figure 15. Size distribution of 15% boron- 85% aluminum, $d_{32} = 4.43 \mu\text{m}$

Experiments are performed on a dust burner in the same manner described in Soo *et al.* for hydrocarbon-powder mixtures [6] and in Goroshin *et al.* for air-powder mixtures [7]. Photographic and spectral data are collected from the flames

2.1 Boron-aluminum-26% O_2 flame

Even at low concentrations of boron in the 5% B- Al mixtures with air proved difficult to stabilize. The flame would only stabilize at low gas flow rates and because of this, the stabilized flame could only last about a minute before concentration fluctuations quenched the flame. The difference between the stabilized flame of the boron mixture and the pure aluminum are shown in Figure 4. The addition of the boron seems to diminish the presence of the outer diffusion cone seen in the aluminum flame suggesting boron actually hinders the aluminum combustion. This effect also observed in Boichuk *et al.* with boron aluminum mixtures where it was found that the flame speed seemed to decrease much more with boron than an inert loading leading to conclude the boron was actually stealing oxygen [8]. Flame speed and spectral data are not yet available.

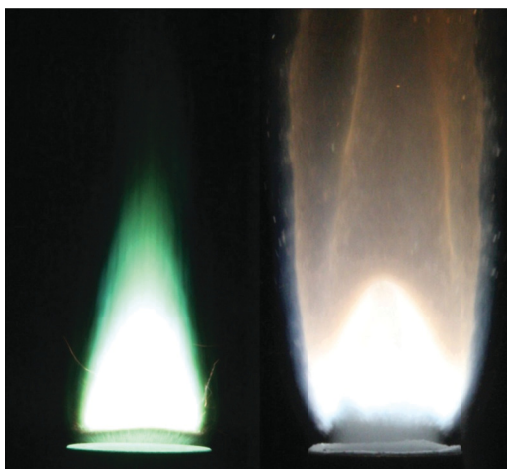


Figure 16. (left) stabilized 5% B- A-air flame, (right) stabilized Al-air flame

2.3Flames in Boron-aluminum-CH₄-26% O₂ mixtures

Previous work on aluminum combustion in hydrocarbon flames showed that increasing the concentration of aluminum powder in the laminar hydrocarbon flame will change the regime of aluminum combustion from slow oxidation to fast combustion of the aluminum [6]. The change is manifested by the formation of an aluminum flame front characterized by a bright white color. In hydrocarbon formulations of aluminum with oxygen excess (i.e., an equivalence ratio of the methane-oxidizer mixture less than 1), the formation of the flame front is still apparent but the diffusion flame surrounding the flame cone is whiter in color due to the oxidation of aluminum in the excess oxygen.

At low concentrations of boron mixture (shown in Figure 5-A2), the appearance of a green diffusion flame around the flame cone is due to the presence of BO₂ gas which is an intermediate gas phase species of boron oxidation. The presence of this green color, and hence BO₂, is evidence of the vaporization of the boron oxide layer on the particle surface. Once the oxide has boiled the boron reacts with the oxygen to form gas phase oxidize which are easily excited in the visual spectrum as shown in Figure 6. The spectrum is dominated by the presence of the vibrational bands of BO₂ A-X state transition. The presence of impurities in the boron is also apparent as the intensities of the K and Na atomic lines are much greater than that seen in Ampal mixtures [6]. These atomic lines lend to the red color of the flame front seen in Figure 5-B2. The vaporization temperature of B₂O₃ is around 2200 K, and when mixture of methane to oxidizer is sufficiently lean to lower the flame temperature below this point, this green color can be effectively 'turned off' despite the increased oxygen present in the mixture. Determination of this effect should be evident in the spectra. Increasing the concentration of the boron-aluminum mixture into the flame seems to have the same effect as increasing concentrations of pure aluminum. At a certain point (shown in Figure 5-C1 and Figure 5-C2), the aluminum front (or boron-aluminum front) forms and comes down over the methane cone. The front is significantly brighter than the methane cone and over shadows the orange color due to particle heating and atomic impurities in the boron as seen from the differences between Figure 5-B2 and the formation of the flame in Figure 5-C2

Even in low concentrations, there is a tendency of the BO₂ emission to dominate over the continuum from particle heating. Figure 6 is a spectrum taken between Figure 5-B2 and Figure 5-C2. Because of the dominance of the gas phase emission it becomes difficult to take a multi-color temperature measurement of the particles in the visual spectral range.

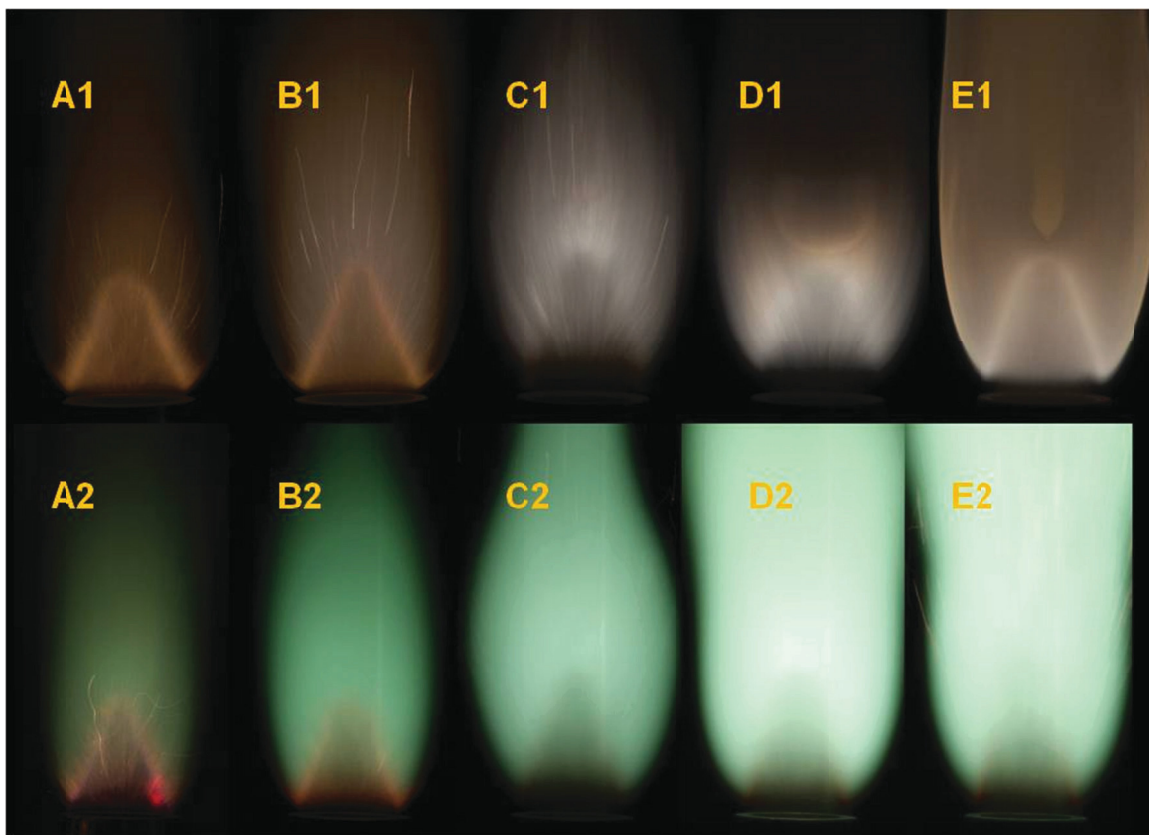


Figure 17. (top) progression of flame in a CH₄-Al-26% O₂ flame from low concentration in A1 to high concentration in E1. C1 shows the formation of the aluminum flame front. (below) progression of flame in a CH₄-15%B-Al-26% O₂ flame from low concentration in A2 to high concentration in E2. C2 shows the formation of the aluminum or aluminum-boron flame front.

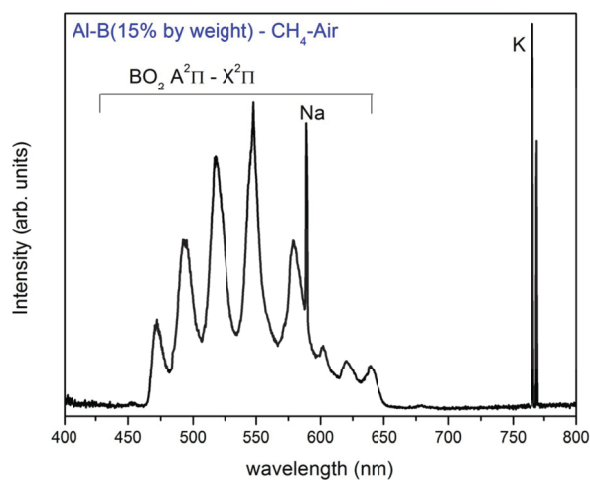


Figure 18. Spectra of the flame in boron-aluminum-methane mixture. The BO₂ transitions dominate the spectra with rather high K and Na impurities.

At higher concentration of powder, the aluminum loaded flame will form a well defined flame cone as it fully couples to the hydrocarbon front shown in Figure 7 [6]. The boron mixture has an obscured flame front due to

the BO_2 emission in the diffusion flame surrounding the flame cone. The molecular emission even obscures the characteristic AlO vibrational bands indicating the fast combustion of aluminum. This also renders an AlO temperature measurement impossible. Figure 8 shows some of the AlO structure obscured by the BO_2 bands. Higher concentrations of the boron mixture tend to cause agglomeration in the dispersion which is apparent in Figure 7 where the white lines depicted in the diffusion cone of the boron mixture are the agglomerated boron particles.



Figure 19. (left) $\text{Al}-\text{CH}_4$ flame at high concentrations of powder. (right) B-Al-CH_4 at high concentrations of powder (with agglomerates)

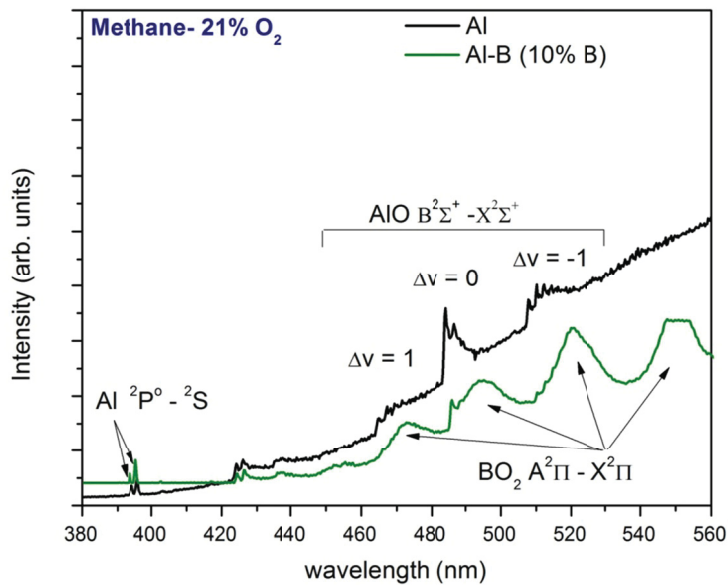


Figure 20. AlO bands being obscured by the BO_2 emission.

2.3.1 Flame speed

The flame speed measurement is performed using the same procedure for Bunsen cones in past studies [6]. The resulting flame speed measurements in the boron mixtures compared to the aluminum case are shown in

Figure 9. The same behaviour was observed as in the case of pure aluminum in a methane flame [6]. The flame speed first decreases with an increase in concentration. This is an indication that the particles act as an inert heat loading which decreases the flame speed. The flame speed then plateaus and remains stable with increasing powder concentration.

The first results indicate that the flame speed in the boron mixture is similar to that in the aluminum case. This is an indication that the boron combustion in the hydrocarbon flames at least does not hinder the aluminum flame front propagation. To check the effect of the boron on the flame speed, the boron can be replaced with an inert material of a similar particle size and heat capacity of boron.

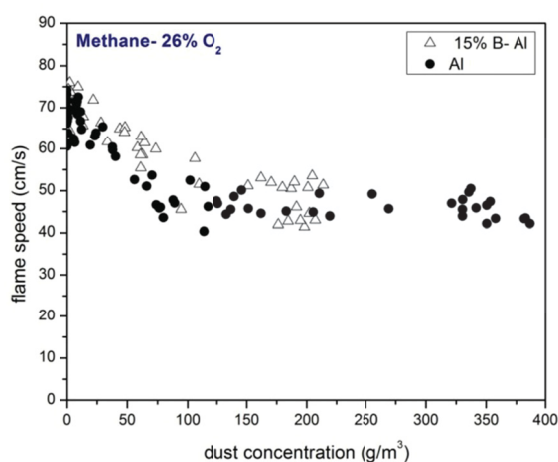


Figure 21. Flame speeds in Al-CH₄ mixtures compared to B-Al-CH₄ mixtures.

2.3.2. Combustion product analysis

The products are collected by passing copper plates over the flame near the flame front for a given range of concentrations. The original powder mixture is sampled as a baseline. Products were collected for flames in the low concentration range and after the formation of the flame front in the high concentration range. A method for separating the remaining boron content from the aluminum is required. Dr Ringuette suggests using XRD/SEM technique or the XPS technique.

2.3.3 Thermodynamic Analysis

The equilibrium temperature calculation in Figure 11 predicts a maximum slightly lower than with pure aluminum powder (see [6] for comparison). Introduction of the boron into the system allows for product formation of the boron with hydrocarbon intermediates.

To maximize the energy output of the boron reaction, it is necessary to force the reaction to yield the most energetic oxide, B₂O₃. In the current formulation, with the addition of the hydrocarbon fuel, the predicted yield of B₂O₃ (shown in Figure 12) falls below 10%, indicating that thermodynamically, only around 10% of the boron product will produce the desired energy output. Aluminum has no significant reactions with the hydrocarbon intermediates and therefore has almost 100% yield of the most energetic oxide in the absence of limiting kinetic rates.

The equilibrium calculation predicts a peak in HOBO and decrease in this intermediate at higher concentrations of dust showing that the concentration effect of dust will have an effect on the formation of the intermediates and possibly faster, more energetic products of boron.

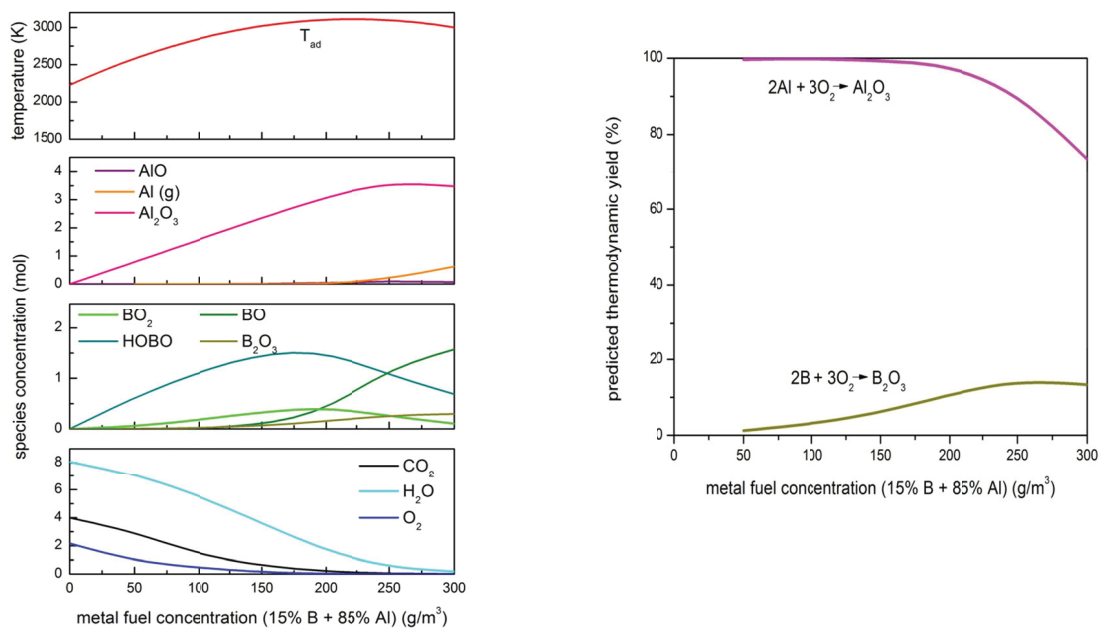


Figure 22. Equilibrium calculation of 15% B-Al-CH₄-26%O₂ for different concentrations of powder.
Figure 23. Percent yield of the most energetic oxide formation from the equilibrium calculation.

References to Chapter II

1. Gany, A. and Y.M. Timnat, Advantages and drawbacks of boron-fueled propulsion. *Acta Astronautica*, 1993. **29**(3): p. 181-187.
2. Goroshin, S., A.J. Higgins, and M. Kamel, Powdered metals as fuel for hypersonic ramjets, in 37th AIAA/ASME/SAE/ASEE Joint Propulsion Conference & Exhibit 2001: Salt Lake City, Utah.
3. Ulas, A., K.K. Kuo, and C. Gotzmer, Ignition and combustion of boron particles in fluorine-containing environments. *Combustion and Flame*, 2001. **127**(1–2): p. 1935-1957.
4. Yeh, C.L. and K. Kuo, Ignition and combustion of boron particles. *Progress in Energy and Combustion Science*, 1996. **22**(6): p. 511-541.
5. Goroshin, S., I. Fomenko, and J.H.S. Lee, Burning velocities in fuel-rich aluminum dust clouds. *Proceedings of the Combustion Institute*, 1996. **26**(2): p. 1961-1967.
6. Soo, M., et al., Stabilized flames in hybrid aluminum–methane–air mixtures [in press]. *Proceedings of the Combustion Institute*, 2012.
7. Goroshin, S., et al., Emission spectroscopy of flame fronts in aluminum suspensions. *Proceedings of the Combustion Institute*, 2007. **31**(2): p. 2011-2019.
8. Boichuk, L., V. Shevchuk, and A. Shvets, Flame propagation in two-component aluminum–boron gas suspensions. *Combustion, Explosion, and Shock Waves*, 2002. **38**(6): p. 651-654.

1. Introduction

The aluminum-water reaction has been widely investigated over the years. In most cases, studies focused on the combustion process of aluminum and steam in two major areas: underwater propulsion technology [1-2] and the high-temperature aluminum combustion in solid propellants [3-4]. During the past few years, other applications of metal-water reactions have emerged, including aluminum-water “green” propellants which possess a specific impulse of around 230 s. These propellants can be used in various fields, and are most prominent in the area of space propulsion [5-7] due to the light hydrogen gas produced during combustion. In combustion-related applications, however, only the thermal part of the energy associated to Al-water reaction is typically used (around 55%), while hydrogen serves merely as the exhaust gas.

For the last decade, another high-profile application of the metal water reaction has emerged: in-situ hydrogen generation, which can be utilized in fuel cells, generators and other devices [8]. This topic has gained growing interest due to global climate change and the need for a clean, non-polluting fuel to replace hydrocarbons. Typically, the devices are operated under atmospheric pressures and at temperatures below the boiling point of water, thus only the hydrogen-air reaction energy is used, and the thermal energy released in the aluminum-water reaction is lost.

Efficient use of metal as an energy carrier requires harvesting the maximum energy that aluminum-water reaction can deliver utilizing both the hydrogen and the thermal energy released during its generation. In order to harness the heat generated during hydrogen production (using a steam turbine, thermoelectric (TE) generator or an externally-heated Stirling-type engine) the reaction has to be performed at temperatures considerably higher than the environment. While the aluminum-water combustion temperature (~3000 K) cannot be handled efficiently in practical devices, reactors operated at several hundred degrees can be designed and used, though elevated pressures are required in order to prevent the water from boiling. However, very limited data are available for the Al-water kinetics in the intermediate temperature regime, and therefore no reliable estimations on the feasibility and performance of such reactors have been published. This study seeks to broaden our understanding of aluminum-water reactions over the temperature range from 20°C to 200°C, where hydrogen production is accompanied by possible utilization of the heat of the reaction.

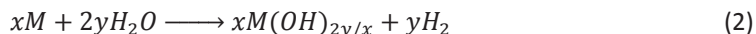
2. Background

Metal-water reactions enable the production of hydrogen on demand, thus bypassing some of the disadvantages related to the use of elemental hydrogen [8]. This method is relatively safe and inexpensive, requires no hydrogen cooling and pressurization, and the volumetric hydrogen content in water is more than 50% higher than it is in the form of pure liquid hydrogen (111 vs. 71 kg/m³) [9] – a solution to the severe storage issues resulting from hydrogen’s low volumetric energy density.

A complete reaction between metal and water can be described as follows:



where x and y are determined by the metal’s ion charge. However, in some cases, especially at relatively low temperatures, intermediate products can also be obtained (mainly metal-hydroxides) and the metal is not fully oxidized. In these cases, however, hydrogen yield is expected to stay unchanged, as long as enough water is available to react, as seen in Eq. 2:



Studies have investigated the metal-water reaction for several metals, such as aluminum, zinc and magnesium [10-16]. Among these metals, aluminum was found to be the most appropriate for hydrogen production due to its highly positive ion (+3), low price, and abundance in the Earth’s crust. The recycling technologies from aluminum oxide to aluminum are also very mature and inexpensive, and are used extensively in the aluminum industry. Table 1 shows that compared to other common metals, aluminum will produce the highest hydrogen yield, both gravimetrically and volumetrically.

Table 1: Gravimetric and volumetric hydrogen yield for different metals

Metal	Mg	Al	Fe	Cu	Zn
Atomic mass [amu]	24.3	<u>27</u>	55.8	63.5	65.4
Density [g/cm ³]	1.74	<u>2.70</u>	7.87	8.96	7.14
Hydrogen produced from 1 kg of metal [mol]	41	<u>56</u>	18	16	15
Hydrogen produced from 1 dm ³ of metal [mol]	72	<u>150</u>	141	141	109

Most of the recent publications studied Al-water kinetics at temperatures below the boiling point of water and at low pressures [17-33]. This relatively low reaction temperature results in poor reaction rates and hydrogen yields due to the protective aluminum oxide layer. Several methods have been used in order to overcome this limitation. The most common method studied to date is the use of alkali hydroxide additives [17-20], which allow water penetration through the alumina layer and accelerate hydrogen production. However, the corrosive and potentially dangerous nature of alkali hydroxides is undesirable. Aluminum alloys were also considered as reaction promoters [21-25] due to the addition of reactive metal catalysts. High reaction rates were reported for several compositions, but the decrease in potential hydrogen yield, the low availability of the metal additives [25] and the increased complexity due to the seeding process make this method unattractive. A different and unique approach to overcome the passive alumina layer was employed by Rosenband and Gany [26]. They used a small fraction of lithium-based activator to form an activated aluminum powder, which undergoes a spontaneous reaction with water. They reported a fast, self-sustained reaction of activated aluminum with water even at room temperature, and practically 100% yield of hydrogen generation in some cases. They showed that the reaction rate may be controlled by the aluminum particle size, water temperature, metal activation conditions, and metal/water mass ratio.

Other studies investigated the use of nano aluminum, and reported enhanced reaction rates [27-28]. However, the low percentage of available active aluminum in the nano powder, its high price, and the relatively fast degradation and oxidation of the powder make nano aluminum less favorable in terms of commercial hydrogen production. Another novel approach to accelerate the metal-water reaction involves ultrasonic agitation of the Al-water mixture. This method has yet to be used and no previous studies on the subject have been published. It is believed that better mixing will increase the interaction between metal powder particles and the surrounding water environment, leading to higher reaction rates and increased hydrogen yields. The proposed method, if proven effective, could eliminate the need for reaction catalysts and additives that are now widely used for the enhancement of hydrogen production rate.

The exact mechanism of the Al-water reaction is not fully understood, though it is believed the chemical reaction at temperatures up to 280°C follows the scheme shown in Eq. 3 to produce Bayerite (Al(OH)₃) in addition to hydrogen [29]:



This was supported by Bunker et al. [30], who used Secondary Ion Mass Spectrometry (SIMS) to examine the passive oxide layer of aluminum particles. They reported high concentration of hydroxides in the passive aluminum oxide film, suggesting that hydration of that film plays an important role in mediating its properties. Deng et al. [31] and Deng et al. [32] proposed a model explaining the different stages in Al-water reaction leading to the final one-step reaction described in Eq. 3:

1. At the aluminum particle surface, the oxide layer is hydrated and Boehmite is formed:



2. At the AlOOH:Al₂O₃:Al interface, aluminum and Boehmite produce alumina and hydrogen bubbles:



3. The non-reacted Boehmite reacts with excess water, if present, to produce Bayerite:



They speculated that the pressure difference between the trapped hydrogen bubbles and the environment results in failure of the hydrated layer, allowing water to come in contact with the aluminum core and restart the described process. For 3 μm powder, they showed increasing hydrogen production with temperature (up to 50°C) under near-vacuum conditions but, surprisingly, almost no production at 75°C and at atmospheric pressure.

Many studies have tried to establish the activation energy (E_a) of the Al-water reaction. Ivanov et al. [27] performed Al-water experiments at the 50-75°C temperature range, using ultra-dispersed particles with specific surface of 5-25 m²/g, corresponding to particle diameter of 90-450 nm. They observed an increasing reaction rate

with temperature (from 30 to 330 cm³/min/g_{Al}) and a decrease in reaction induction time with temperature (from 78 min at 50°C to 2.5 min at 75°C), and calculate the reaction activation energy to be 85 kJ/mol. Lyashko et al. [28] studied the reaction of water with different powders in the 130-270 nm range, and reported activation energies of 54-100 kJ/mol. They, however, used data from only two temperatures, 45°C and 60°C, which together with the wide range of reported E_a values, suggests high uncertainty in the E_a values obtained. Studart et al. [33] investigated the Al-H₂O kinetics for cement casting processes. They offered a four-stage reaction mechanism explaining hydrogen generation from aluminum-water reaction. They suggested that the two most dominant parameters controlling hydrogen production are the PH level and the Al(OH)₄⁻ ion concentration in the aqueous solution. Their experimental results were analyzed to estimate the activation energy of Boehmite (AlOOH) and Bayerite (Al(OH)₃), and values of 62 kJ/mol and 53 kJ/mol, respectively, were reported. In general, the relatively narrow temperature range in these studies (20-75°C) leads to considerable uncertainty regarding the reported values for activation energy.

Although showing useful and promising results, low temperature Al-water reaction is somewhat limiting, since it requires the use of additives or other methods in order to overcome the passive oxide shell. The narrow experimental temperature range in previous studies (20-80°C) limits the degree of certainty of the extracted reaction properties, mainly activation energy. As mentioned, it also precludes the utilization of heat generated during metal-water reaction, so more than half (54-56%) of the reaction energy is lost. Working at higher temperatures is expected to enhance the hydrogen production rate, leading to a reduced need for additives or nano powders. The experimental work conducted by Laritchev *et al.* [34] studied aluminum reaction with water (up to 100°C) and water vapor (up to 900°C). They report that full oxidation of aluminum with water and water vapor is achieved during a reasonable time (up to 60 minutes) for micron and submicron powders, as well as for flakes less than one micron thick. They note that the composition of solid reaction products depends on the average size of Al particles, and changes from Al(OH)₃ for the micron size particles to AlOOH for the submicron and flake aluminum. Although showing similar trends between the results for water and for water vapor, there is still a gap with regards to the behavior of aluminum-water mixtures for temperatures higher than 100°C. Water vapor also possesses much lower density, making the use of it less attractive. Potapova et al. [35] investigated the kinetics of aluminum oxidation by water vapor at 150-250°C range and steam pressure of 500-5000 kPa. In their 0.5-6.5 hr long experiments they used 24 µm aluminum particles, and extracted reaction order and activation energy from their results. They calculated E_a to be as low as 10 kJ/mol.

Despite a lack of experimental data for aluminum-water reactions at intermediate temperatures, the benefit of utilizing the reaction heat as part of a power cycle has been noted in prior studies. An analysis of the combined hydrogen-production/power-generation concept was made by Franzoni et al. [36]. They estimated the energy conversion efficiency of a power system based on Al-H₂O combustion when adopting a superheated steam cycle or a combined heat and power cycle. In both cases, the efficiency ranges between 0.62 and 0.85, assuming that the hydrogen produced by the system is then employed in a fuel cell. Barone et al. [37] extended this idea into a feasibility study of using the aluminum-water reaction to power unmanned underwater vehicles (UUVs). They showed analysis of several proposed systems including different engines (Stirling, steam or TE generator) and various uses for the produced hydrogen. They estimated the specific energy obtained from the system to be 800-1600 (W-hr)/kg, well beyond the 600 (W-hr)/kg long-duration mission requirement defined in their study.

This paper investigates aluminum-water reactions over a wide temperature range (20-200°C). Little is known on the behavior and characteristics of the Al-water reaction in this temperature range, and this study aims at filling some of these gaps. The effect of particle size on the reaction characteristics has yet to be fully explored, and the current research examines the effect of this parameter through the use of three different particle sizes. In addition, results for Al-water experiments where ultrasonic agitation is used are presented and discussed. A simple physical mechanism is proposed to explain the effects of reaction temperature and particle size on the reaction yield.

3. Experimental setup

The present apparatus is designed to enable measurements of the main characteristics of the reaction, hydrogen production rate and hydrogen yield, as a function of temperature. The setup consists of a high-pressure reactor, where metal powder reacts with high temperature, pressurized water to release hydrogen. High pressure, which is

essential for keeping water in its liquid state at high temperatures, is achieved by allowing a reference hydrogen backflow through the reactor and adjusting a relief valve situated at the top of the reactor to the desired pressure. The produced and backflow hydrogen travel through a bubbler condenser filled with cold icy water in order to condense any steam remaining in the flow into liquid water. The hydrogen then flows through a flowmeter which is connected to a data acquisition system. Backflow hydrogen is also measured before entering the reactor, thus enabling the calculation, by simple subtraction, of the hydrogen produced by the metal-water reaction. Schematics of the general apparatus and the high-pressure reactor are given in Figs. 1a and 1b, respectively.

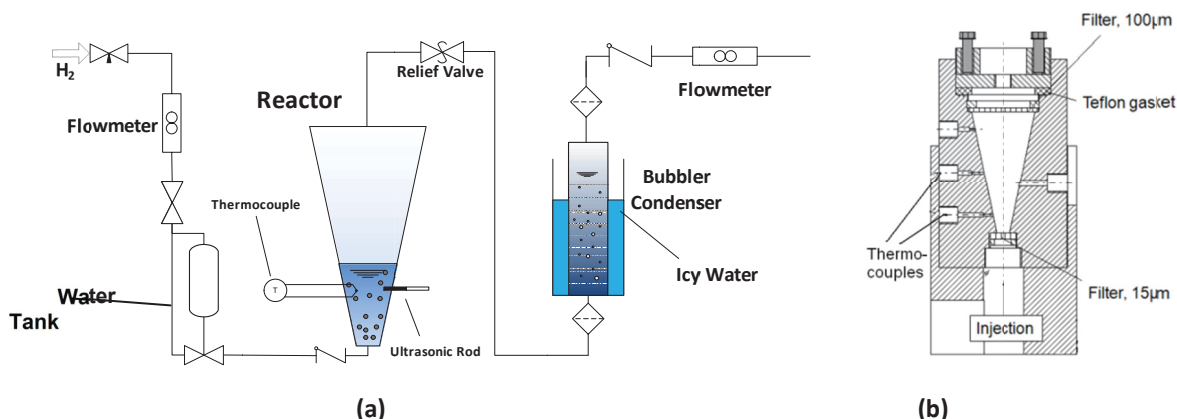


Figure 1: A schematic drawing of (a) the reactor and (b) the apparatus. Backflow hydrogen bubbles through the reactor and pressure is controlled through a relief valve.

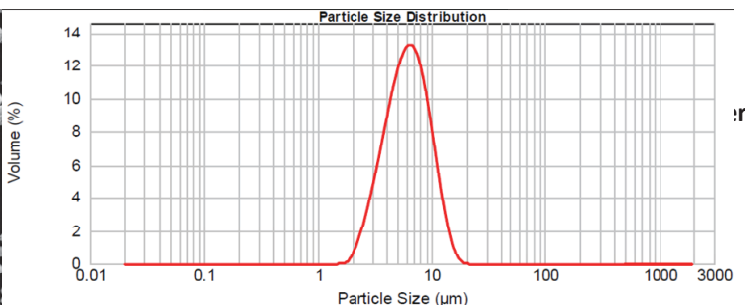
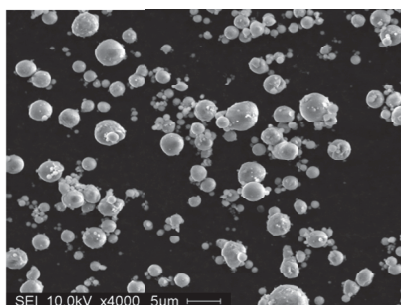
The aluminum powder mass used in the experiments was in the range of 0.2-0.5 g, while the surrounding water mass was typically 20 g. In these conditions, water is in much excess in the reactor, since a stoichiometric mixture comprises of two grams of water per each gram of aluminum, as can be determined from Eq. 3. The water-rich mixture was employed for two main reasons: in order to enable complete aluminum oxidation, and to maintain constant temperature despite the exothermic reaction.

The metal-water reactor, as well as the water tank, were situated in an aluminum block which was heated through a heating plate and heating pads. When the desired experiment temperature was reached, aluminum powder was poured into the reactor. The reaction was then initiated by injecting the preheated, pressurized, distilled water to the reactor, and efficient stirring of the mixture was achieved by bubbling the reference hydrogen flow through the reacting slurry bed inside the conical reactor. In every experiment, the Al-water mixture temperature was measured via K-type thermocouples, the hydrogen flow was monitored with *Omega FMA* flowmeters, and readings were acquired with a *PDAQ* data acquisition system every 0.5 second. Experimental temperatures were in the range of 20-200°C.

Spherical aluminum powders at different sizes were used during the experiments. Table 2 details their mean volumetric diameter, as well as their specific surface and manufacturer. The majority of experiments were conducted with H-2 and H-10 powders. Figures 2 and 3 show SEM images of these powders, as well as their fairly narrow size distributions. Figure 4 shows a TEM image of the nanosize ALEX powder, as well as its size distribution.

Table 2: Aluminum powders used in this study

	Powder name	Manufacturer	$d_{0.5}$ [μm]	Specific surface [m^2/g]
1	ALEX	APT	0.12	18.5
2	H-2	Valimet	6.0	0.37
3	H-10	Valimet	13.8	0.16



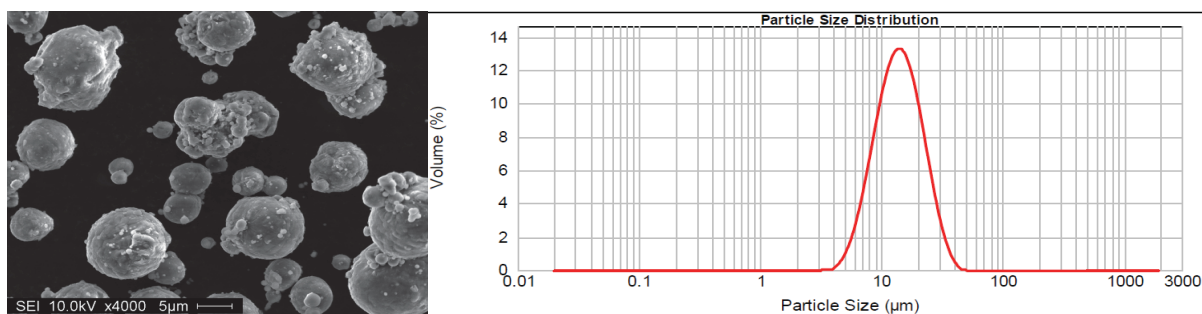


Figure 3: SEM image (a) and volumetric size distribution (b) of H-10 aluminum powder.

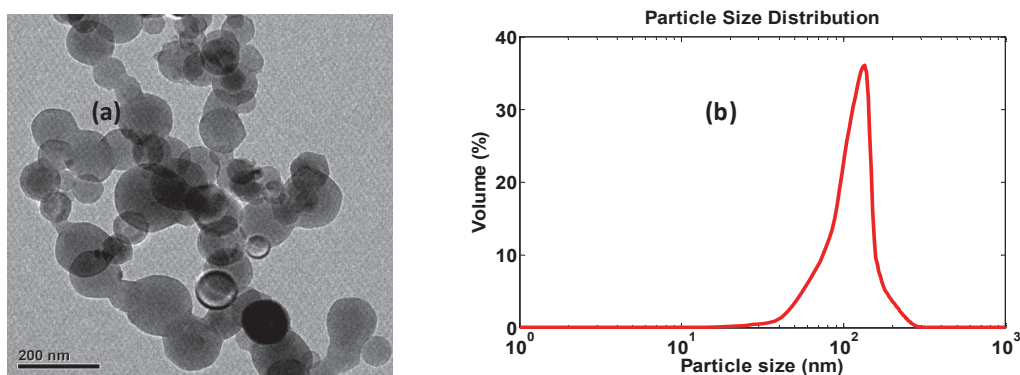


Figure 4: TEM image (a) and volumetric size distribution (b) ALEX aluminum powder.

In order to explore the effects of ultrasonic agitation, several experiments included an ultrasonic rod (sonorode) connected to the reactor via a 7 mm port (see Fig. 1b), and sealed with an O-ring between the sonorode and a brass sleeve. The rod was connected to a *UP50H Hielscher* ultrasound processor, enabling ultrasonic vibration at power levels up to 50 W. The ultrasound setup was not designed to hold pressures higher than atmospheric pressure, therefore the temperature in ultrasound experiments was limited to a maximum of 90°C. In this study, the ultrasonic processor was operated at a power of 30 W during the experiments.

4. Results

Experiments were performed with different powders over a range of temperatures. An example for data taken from experiments conducted with H-2 powder at several temperatures is given in Fig. 5. In all three cases an induction time is observed, in which it is believed that the passive oxide layer starts to hydrate and decompose. Following that, hydrogen generation commences until reaching peak production, followed by a sharp decay of the production rate and termination of the reaction.

a. Reaction temperature

Increasing reaction temperature, as seen in Fig. 5, results in a faster Al-water reaction and a higher flow rate of produced hydrogen, as expected due to Arrhenius-type behavior. A time-to-peak, τ , is defined as the time to reach maximum hydrogen production rate. As reaction temperature increases, it can be noted that the time-to-peak, τ , is decreased.

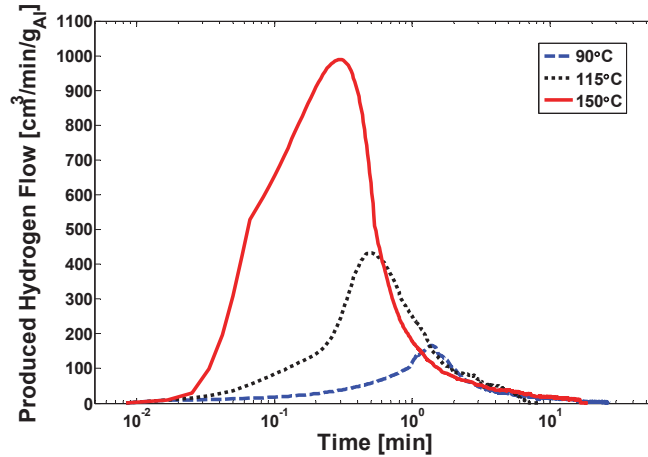


Figure 5: Produced hydrogen flow rate vs. time for experiments conducted with H-2 aluminum powder at different temperatures.

When integrating the curves shown in Fig. 5 with time, one can obtain the hydrogen yield for each case, which is proportional to the area under the hydrogen flow curves. Figure 6 shows the total hydrogen yield in experiments conducted with the same powder (H-2) at various temperatures. Higher reaction temperature is expected to increase the reaction rate and shorten the time-to-peak, but the observed trend of increased yield with temperature shown in Fig. 6 suggests an additional clear advantage for conducting Al-water reaction at high temperatures. The recorded higher hydrogen yield indicates enhanced reaction efficiency, making it more attractive for use in commercial systems. It may also allow the use of micron size particles, rather than nano powders, without affecting overall system performance.

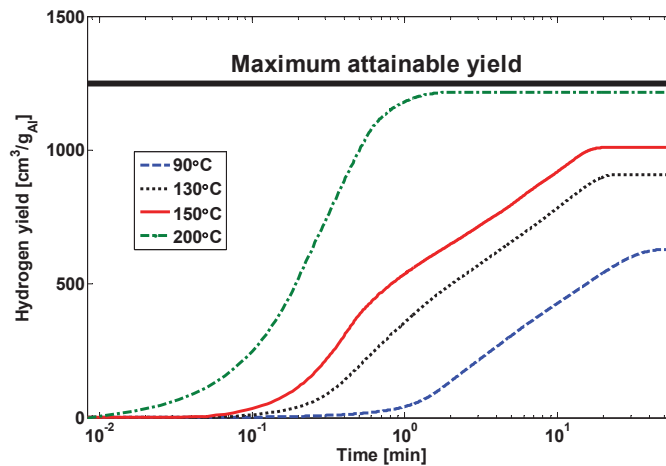


Figure 6: Hydrogen yield vs. time at various temperatures for experiments conducted with H-2 aluminum powder.

b. Particle size

The effect of aluminum particle size on the Al-water reaction was studied using three different powders. The larger flow rate for the smaller H-2 powder compared to the H-10 powder is presented in Fig. 7. It is clear that the Al-water reaction with smaller aluminum particles (H-2) produces hydrogen at a higher rate, and also results in larger total yield. The larger specific surface of the smaller powder leads to increased reaction rates. The increased reaction completeness, i.e. total yield, is an additional benefit of smaller particles.

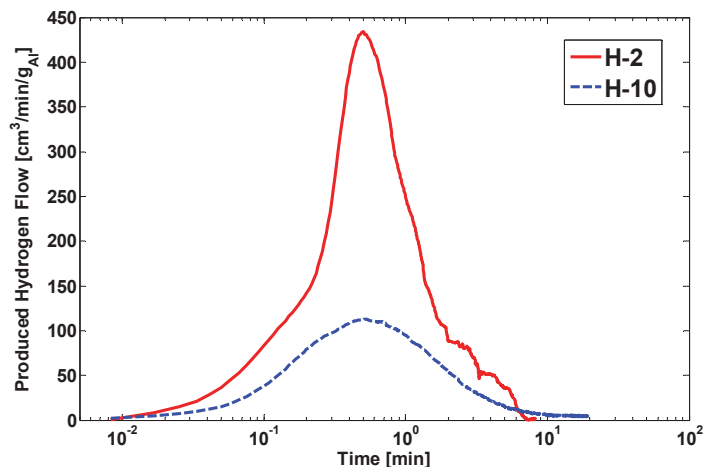


Figure 7: Produced hydrogen flow rate vs. time for experiments conducted at 115°C with H-2 (6 μm) and H-10 (13.8 μm) aluminum powders.

The observed trend of higher hydrogen production for smaller powder (H-2 vs. H-10) was also examined during experiments conducted with nano size aluminum powder (ALEX). Figure 8 shows a dramatic increase in hydrogen generation for the nano-scale powder for experiments conducted at 70°C. The total hydrogen yield in this experiment (nano size particles, 70°C) reached 98%, meaning the aluminum powder had reacted almost fully with the surrounding distilled water. The recorded maximum flow rate in this experiment is almost four times larger than that of [27], which was conducted in a similar temperature. The large difference is probably due to the slightly different particle size – 120 nm in this study vs. 90-450 nm in [27]. It could also stem from the relatively fresh powder used in this work (2-3 months after production) since nano size powders may quickly degrade and oxidize if not sealed and stored well. The high reactivity of ALEX powder was also noticed during the experiments conducted at 100°C and 115°C. In these experiments, thermal runaway was observed, as the temperature in the reactor rapidly increased by 60-70°C due to the fast Al-water reaction. The hydrogen flowmeter displayed saturated values not only due to the high hydrogen flow but also due to the rapid boiling of water into steam, resulting from the sudden increase in temperature, which overwhelmed the capabilities of the bubbler-condenser used. Obviously, flow rate measurements from these two experiments cannot be considered during data processing, although it is safe to argue that hydrogen yield reached practically 100% for these cases. Thermal runaway was not observed in the ALEX experiment conducted at 90°C, indicating that the runaway limit for this powder lies between 90-100°C.

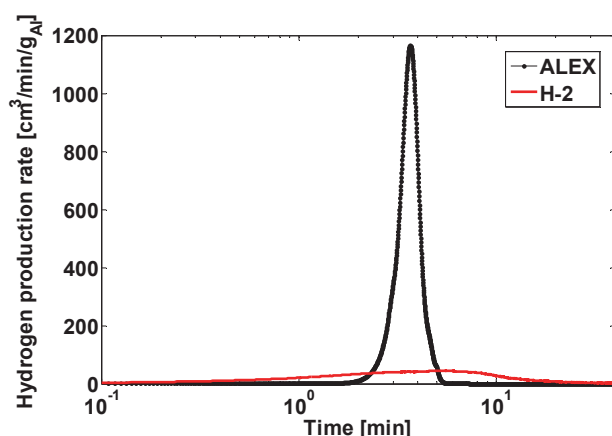


Figure 8: Produced hydrogen flow rate vs. time for experiments conducted at 70°C with ALEX (nano-Al, 0.12 μm) and H-2 (6 μm) aluminum powders.

c. Production rate

The maximum production rates measured during the experiments were plotted versus inverse temperature for H-2, H-10 and ALEX powders. The exponential behavior is seen well in the semi-logarithmic plot of Fig. 9. It is

observed that all three powders follow the Arrhenius behavior, resulting in fairly linear curves on the semi-log plot. The slopes of the three curves seem very similar, implying E_a is not a function of particle size. As expected, smaller particle powders experience higher flow rate throughout the temperature range.

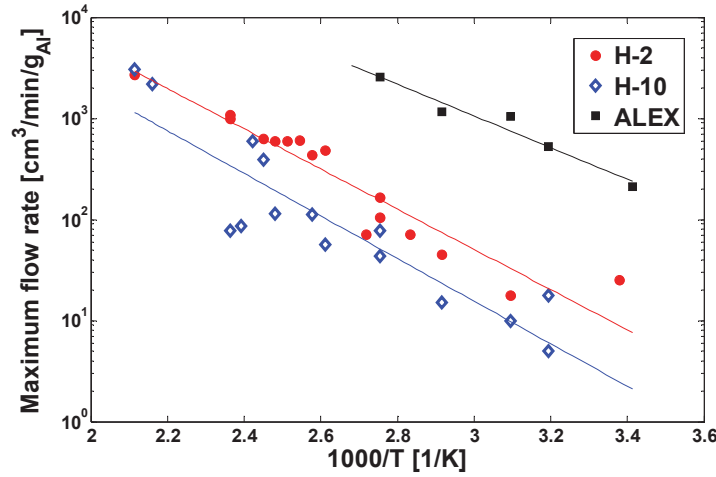


Figure 9: Maximum hydrogen production rate vs. inverse reaction temperature for experiments conducted with H-2, H-10 and ALEX aluminum powders.

Since the aluminum-water reaction is primarily a surface reaction, it is interesting to normalize the recorded flow rates by the sample surface area, rather than by mass. The semi-logarithmic plot in Fig. 10 shows the maximum hydrogen flow per aluminum area vs. inverse temperature. Here, all three powder data collapse narrowly into very similar values, substantiating the claim that the reaction between water and aluminum particles has a significant dependence on surface area, i.e. powder particle size. The consistent trend appearing in Fig. 10 enables the prediction of flow rate for a given operating temperature and particle size. This can lead to better, more accurate design of Al-water systems, depending on the needed hydrogen flow rate. For an increased production rate, one can choose to apply any of the three well-understood parameters: increase reaction temperature, use smaller size powder, or increase the amount of powder.

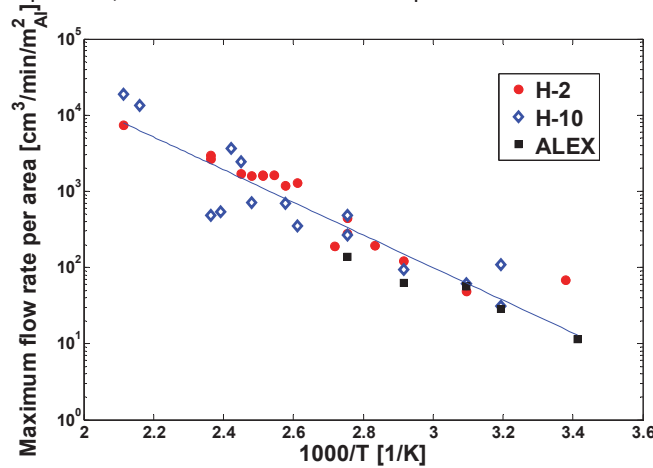


Figure 10: Maximum hydrogen production rate per aluminum area vs. inverse reaction temperature, for experiments conducted with H-2, H-10 and ALEX aluminum powders.

The collected data presented in Fig. 10 is used to calculate the activation energy of the reaction E_a using the linear slope, since the reaction rate typically follows the equation:

$$w = w_0 \cdot e^{-\frac{E_a}{R_0 T}} \quad (7)$$

where w is the hydrogen production rate, given in units of $\left[\frac{\text{cm}^3}{\text{min} \cdot \text{m}^2_{\text{Al}}}\right]$, R_0 is the universal gas constant ($R_0 = 8.314 \frac{\text{J}}{\text{mol} \cdot \text{K}}$) and T is the reaction temperature. The calculated activation energy, which was independent of particle size, was found to be $41 \pm 5.3 \text{ kJ/mol}$, and the pre-exponential factor w_0 was calculated to be $2.65 \cdot 10^8 \frac{\text{cm}^3}{\text{min} \cdot \text{m}^2_{\text{Al}}}$, with 95% confidence interval in the range of $4.63 \cdot 10^7 < w_0 < 1.52 \cdot 10^9$. The value obtained for E_a is slightly lower than those reported by [26-28, 33] (53-85 kJ/mol), but is based on a much wider temperature range (180°C vs. 55°C), as well as on powders of different particle size.

d. Hydrogen yield

The hydrogen yield was determined by integrating the hydrogen flow with time, and was normalized by the maximum attainable theoretical yield that results from Eq. 3, which is $1249 \frac{\text{cm}^3}{\text{min} \cdot \text{g}_{\text{Al}}}$. It was found that for H-2, H-10 and ALEX powders, hydrogen yield increases with reaction temperature, as seen in Fig. 11.

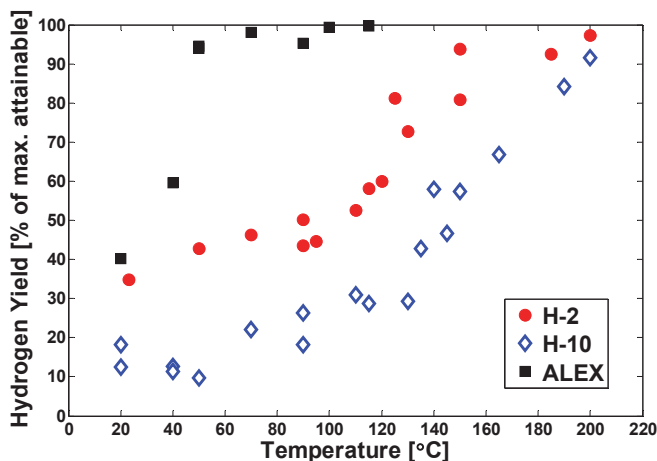


Figure 11: Hydrogen yield vs. reaction temperature for experiments conducted with H-2, H-10 and ALEX aluminum powders.

Higher yield was observed in experiments conducted with H-2 powder compared to experiments conducted with H-10 powder throughout the temperature range. In the nano-powder experiments, the recorded yield was almost 100% at temperatures higher than 50°C. Figure 11 demonstrates the advantage of using smaller aluminum particles at a given temperature, showing a clear gap in hydrogen yield between the three powders. Nevertheless, high yield efficiencies were observed for the large H-10 powder at high temperatures, making it an attractive candidate for commercial use due to its lower price and high active aluminum content. It can be seen that for each powder, close to 100% yield is reached at a different temperature, suggesting the existence of an optimal reaction temperature as a function of particle size. This can exclude the need for hydroxide additives or other methods previously used to enhance production, thus making the process much simpler and less expensive.

e. Ultrasonic agitation

Effects of ultrasonic agitation on hydrogen production were also explored in this study. A *UP50H Hielscher* ultrasound processor was used in experiments conducted with H-2 and H-10 powders, agitating the Al-water mixture at a constant power of 30 W. The temperature in these experiments (with ultrasound, denoted US) ranged up to 90°C, due to the apparatus limitations discussed previously. Figure 12 demonstrates the effect of ultrasound on hydrogen generation, showing data from H-10 experiments at 90°C, with and without ultrasound. It can be seen that hydrogen peak production is significantly higher for the experiment conducted with ultrasonic agitation (181 vs. 78 $\text{cm}^3/\text{min}/\text{g}_{\text{Al}}$). When calculating total yield for both experiments, a substantial difference is also noticed – 41% of maximum attainable hydrogen for the US experiment versus 26% for the experiment conducted without ultrasound.

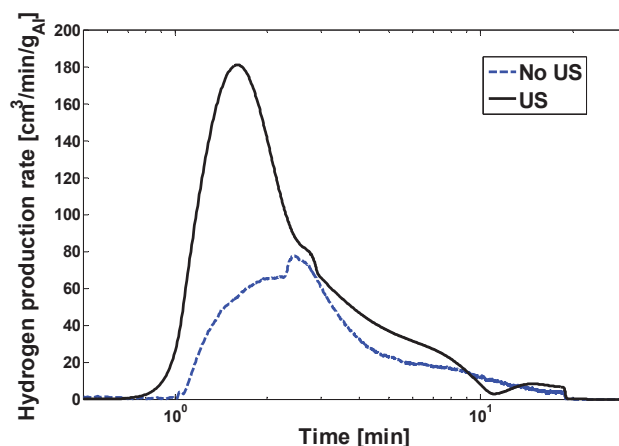


Figure 12: Produced hydrogen flow rate vs. time for experiments conducted at 90°C with H-10 (13.8 μm) aluminum powder, with and without ultrasonic agitation.

The behavior observed in Fig. 12 repeated throughout the 20-90°C temperature range, for both H-2 and H-10 powders. In most experiments, maximum production rate experienced a notable increase due to ultrasound use, but more importantly – a distinct rise in hydrogen yield was observed for these experiments compared to the non-US experiments at the same temperature and with the same powder. A clear yield increase in the US experiments is shown in Fig. 13, for the H-2 (13a) and H-10 (13b) powders. It can be seen that for both powders, the use of ultrasonic agitation in Al-water reaction is equivalent (yield-wise) to experiments conducted at temperatures 60-80°C higher. It is believed that the ultrasound vibrations create cracks in the protective oxide layer surrounding the aluminum particle, thus exposing more aluminum sites to freely react with the excess water. Moreover, ultrasonic agitation promotes the discharge of hydrogen bubbles trapped inside the aluminum particle, and by that increases recorded yield. The use of ultrasound also damages the weak external hydrated layer, resulting in the removal of parts of that aluminum hydrate layer. This makes the effective particle diameter smaller and promotes hydrogen release, thus increasing the recorded yield.

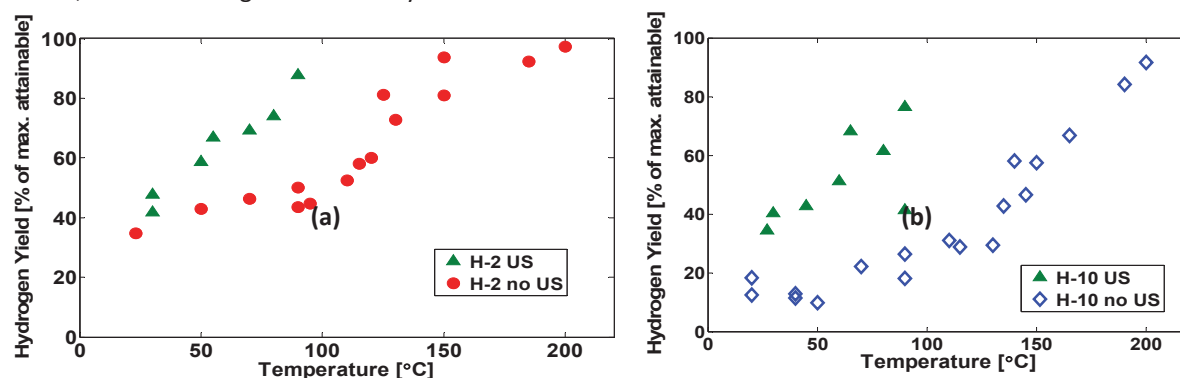


Figure 13: Hydrogen yield vs. reaction temperature for experiments conducted with H-2 (a) and H-10 (b) aluminum powders, with and without ultrasonic agitation.

5. Discussion

Data obtained throughout the experiments clearly indicate that hydrogen yield changes with both aluminum particle size and reaction temperature, and in many cases fails to reach 100%. This implies the existence of an inhibitive mechanism which prevents the aluminum from reacting completely with the surrounding water, leaving an unreacted aluminum core in the middle of the particle. A penetration thickness, t_c , is defined as the distance from the particle edge to the unreacted aluminum core (Fig. 14). Its value represents the maximal hydrated layer thickness for which hydrogen production is not negligible.

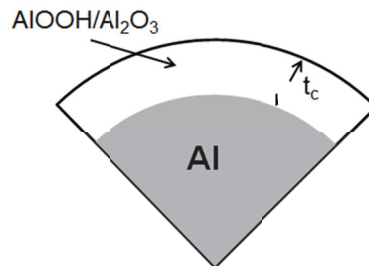


Figure 14: Schematic description of aluminum particle and a penetration thickness t_c . The unreacted aluminum core results in a hydrogen yield of less than 100%.

Figure 15 presents the calculated penetration thickness for H-2 and H-10 experiments in this study, based on yield results. The relative yield (out of 100%) corresponds to the volume fraction of the aluminum that reacted with water. Given that, as well as the mean particle diameter of the powder, penetration thickness can be derived. The value of t_c cannot exceed the particle radius, which is $3\text{ }\mu\text{m}$ and $6.9\text{ }\mu\text{m}$ for the H-2 and H-10 powders, respectively.

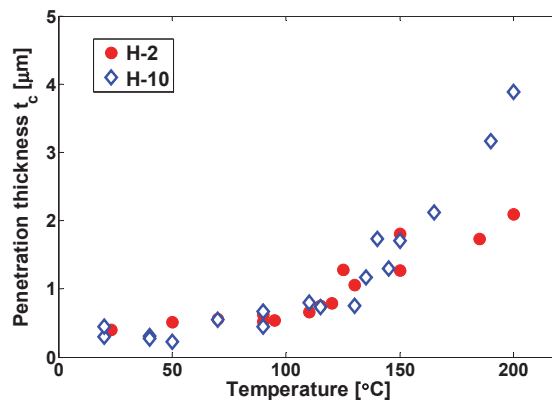


Figure 15: Penetration thickness t_c vs. reaction temperature for experiments conducted with H-2 and H-10 aluminum powders.

It is observed that the penetration thickness t_c calculated for both H-2 and H-10 powders increases with temperature. Furthermore, it is noted that penetration thickness values have little or no dependence on particle size, and collapse for both powders throughout almost all of the temperature range. As the reaction temperature approaches 200°C , the penetration thicknesses for H-2 powder flatten around a value of $2\text{ }\mu\text{m}$, which in terms of yield is very close to the maximum theoretical value – a t_c of $2\text{ }\mu\text{m}$ corresponds to a yield of $\sim 97\%$ ($1 - [1/3]^3$). This result also explains why the nanopowder ($r \approx 60\text{ nm}$) has nearly 100% yield at $T > 50^\circ\text{C}$.

Temperature dependence of the penetration thickness can be attributed to the increased diffusivity of water and oxidizing species with increasing temperature. In addition, the diffusivity of the hydrogen trapped between the aluminum core and the hydrated layer also increases with temperature. This allows higher hydrogen release, resulting in larger penetration thickness and increased flow rate. As seen in Fig. 15, t_c represents a global mechanism which has no dependency on particle size. This implies that coarse aluminum particles will have much larger unreacted core with respect to fine particles (fraction-wise), resulting in lower hydrogen yield. Moreover, for any given operating conditions (namely, reaction temperature), one can choose a powder with particle size so the penetration thickness will reach all the way to the particle center, thus achieving high hydrogen yields and efficiencies.

6. Conclusion

Aluminum-water reactions were investigated for different aluminum powders at various temperatures in a high-pressure reactor. The research examined the behavior of pure Al-water kinetics at intermediate temperatures, a range where only a few studies have been published. It was clearly shown that increasing the reaction temperature is highly favorable in terms of hydrogen production rate, reaction time and total hydrogen

yield. This can lead to a reduced need for reaction-rate enhancers such as alloy additives or corrosive alkali hydroxides. In addition, another clear advantage of working at elevated temperatures is the ability to utilize the heat produced by the exothermic reaction. The results presented in this study suggest that both hydrogen production and heat utilization would experience increased efficiencies from performing reactions at elevated temperatures.

A comparison between the characteristics of aluminum powders with different particle diameter was conducted. It was shown that for the same reaction temperature, a smaller-diameter powder reacted more quickly, had a higher hydrogen production rate, and produced a greater total yield of hydrogen. Therefore, in order to increase reaction performance, one can either increase reaction temperature or use smaller diameter powders. It was found that for each powder, close to 100% yield was reached at a different temperature, suggesting the existence of an optimal reaction temperature as a function of particle size. Hydrogen production rate was shown to have significant dependency on particle size. When normalized by sample surface area, all three powders exhibited similar maximum-flow-rate values for a given reaction temperature. This suggests that the Al-water reaction is controlled by a global mechanism, and possess properties that are universal and independent of particle size. The activation energy of the reaction was calculated using the recorded maximum flow rates per area of all three powders and was found to be 41 kJ/mol. The relatively wide temperature range (180°C) from which E_a was extracted increases the accuracy of its value, compared to values reported in literature which were based on much smaller temperature ranges – spanning from a range of 15°C to a range of 55°C. A formula for the maximum hydrogen production rate per particle surface area as a function of temperature has been proposed, which can be used to assist the design of Al-water reaction systems, as well as to choose appropriate candidate powders for practical devices.

Ultrasonic agitation of the aluminum-water mixture was proven to be an effective method to increase hydrogen production rate, as well as total hydrogen yield. Experiments were performed at temperatures up to 90°C, and the recorded hydrogen yield was found to be similar to the yields of non-ultrasonic experiments conducted at temperatures 60-80°C higher. It is believed that the ultrasound cracks the oxide layer surrounding the aluminum particle and exposes more aluminum sites to freely react with excess water. Moreover, ultrasonic agitation promotes the discharge of hydrogen bubbles trapped inside the aluminum particle, as well as damages and removes some of the weak external hydrated layer. This makes the effective particle diameter smaller and, since penetration thickness (t_c) remains constant, allows the reaction to continue deeper into the particle, which increases the recorded yield.

The penetration thickness, t_c , is a parameter introduced to assess the completeness of the Al-water reaction, and it represents the maximal hydrated layer thickness for which hydrogen production is not negligible. As long as the hydrated layer is thinner than the critical penetration thickness, water or water ions would continue to diffuse and promote hydrogen generation. Penetration thickness is observed to depend on reaction temperature, which controls water (or water ions) and hydrogen diffusivities. At higher temperatures, diffusivities of both oxidizing species and hydrogen increase, resulting in a larger t_c and higher hydrogen yield. Penetration thickness was also shown to have no dependency on particle size, presenting a universal depth of reaction which controls, together with particle diameter, the overall hydrogen yield and reaction efficiency. This discovery, along with the maximum hydrogen production rate expression proposed in this paper, allows the assessment and prediction of production rates and efficiencies for a given aluminum powder and operating temperature, providing important design criteria to hydrogen generation technologies relying on the Al-water reaction.

References to Chapter III

1. Foote JP, Thompson BR, Lineberry JT. Combustion of Aluminum with Steam for Underwater Propulsion. In: Roy GD, editor. *Advances in Chemical Propulsion, Science to Technology*; 2001, p. 133-46.
2. Foote JP, Lineberry JT, Thompson BR, Winkleman BC. Investigation of Aluminum Particle Combustion for Underwater Propulsion Applications. AIAA Paper 96-3086, 1996.
3. Beckstead MW. A Summary of Aluminum Combustion. Presented at the RTO/VKI Special Course “Internal Aerodynamics in Solid Rocket Propulsion”, May 2002, Published in RTO-EN-023.
4. Kudryavtsev VM, Sukhov AV, Voronetskii AV, Shapara AP. High-Pressure Combustion of Metals (Three-Zone Model). *Combust., Explos. Shock Waves* 1979; 15(6): 731-7.

5. Risha GA, Huang Y, Yetter RA, Yang V, Son SF, Tappan BC. Combustion of Aluminum Particles with Steam and Liquid Water. AIAA paper 2006-1154, 2006.
6. Miller TF, Herr JD. Green Rocket Propulsion by Reaction of Al and Mg Powders and Water. AIAA paper 2004-4037, 2004.
7. Ingenito A, Bruno C. Using Aluminum for Space Propulsion. J. Propul. Power 2004; 20(6): 1056-63.
8. Wang HZ, Leung DYC, Leung MKH, Ni M. A Review on Hydrogen Production Using Aluminum and Aluminum Alloys. Renewable Sustainable Energy Rev. 2009; 13: 845-53.
9. Tzimas E, Filiou C, Peteves SD, Veyret JB. Hydrogen Storage: State of the Art and Future Perspective. European Commission, Directorate General Joint Research Centre, Institute for Energy, Petten, the Netherlands, 2003.
10. Wegner K, Ly HC, Weiss RJ, Pratsinis SE, Steinfeld A. In Situ Formation and Hydrolysis of Zn Nanoparticles for H₂ Production by the 2-Step ZnO/Zn Water-Splitting Thermochemical cycle. Int. J. Hydrogen Energy 2006; 31(1): 55-61.
11. Vishnevetsky I, Epstein M. Production of Hydrogen from Solar Zinc in Steam Atmosphere. Int. J. Hydrogen Energy 2007; 32(2): 791-802.
12. Cho CY, Wang KH, Uan JY. Evaluation of a New Hydrogen Generating System: Ni-Rich Magnesium Alloy Catalyzed by Platinum Wire in Sodium Chloride Solution. Mater. Trans. 2005; 46(12): 2704-8.
13. Grosjean MH, Zidoune M, Roue L, Huot JY. Hydrogen Production via Hydrolysis Reaction from Ball-Milled Mg-Based Materials. Int. J. Hydrogen Energy 2006; 31(1): 109-19.
14. Grosjean MH, Roue L. Hydrolysis of Mg-Salt and MgH₂-Salt Mixtures Prepared by Ball Milling for Hydrogen Production. J. Alloys Compd. 2006; 416(1-2): 296-302.
15. Uan JY, Cho CY, Liu KT. Generation of Hydrogen from Magnesium Alloy Scraps Catalyzed by Platinum-Coated Titanium Net in NaCl Aqueous Solution. Int. J. Hydrogen Energy 2007; 32(13): 2337-43.
16. Martinez SS, Benites WL, Gallegos AAA, Sebastian PJ. Recycling of Aluminum to Produce Green Energy. Sol. Energy Mater. Sol. Cells 2005; 88(2): 237-43.
17. Hiraki T, Takeuchi M, Hisa M, Akiyama T. Hydrogen Production from Waste Aluminum at Different Temperatures with LCA. Mater. Trans. 2005; 46(5): 1052-7.
18. Belitskus D. Reaction of Aluminum with Sodium Hydroxide Solution as a Source of Hydrogen. J. Electrochem. Soc. 1970; 117(8): 1097-9.
19. Soler L, Macana's J, Mun~oz M, Casado J. Hydrogen Generation from Aluminum in a Non-Consumable Potassium Hydroxide Solution. Proceedings of the International Hydrogen Energy Congress and Exhibition, IHEC 2005, Istanbul, Turkey, 13-15 July 2005.
20. Hiraki T, Yamauchi S, Iida M, Uesugi H, Akiyama T. Process for Recycling Waste Aluminum with Generation of High-Pressure Hydrogen. Environ. Sci. Technol. 2007; 41(12): 4454-7.
21. Kravchenko OV, Semenenko KN, Bulychev BM, Kalmykov KB. Activation of Aluminum Metal and its Reaction with Water. J Alloys Compd 2005; 397: 58-62.
22. Uehara K, Takeshita H, Kotaka H. Hydrogen Gas Generation in the Wet Cutting of Aluminium and its Alloys. J Mater Process Technol 2002; 127: 174-7.
23. Fan MQ, Xu F, Sun LX. Studies on Hydrogen Generation Characteristics of Hydrolysis of the Ball Milling Al-based Materials in Pure Water. Int J Hydrogen Energy 2007; 32: 2809-15.
24. Fan MQ, Xu F, Sun LX, Zhao JN, Jiang T, Li WX. Hydrolysis of Ball Milling Al-Bi-hydride and Al-Bi-salt Mixture for Hydrogen Generation. J Alloys Compd 2008; 460(1-2): 125-9.
25. Soler L, Macana's J, Mun~oz M, Casado J. Aluminum and Aluminum Alloys as Sources of Hydrogen for Fuel Cell Applications. J Power Sources 2007; 169(1): 144-9.
26. Rosenband V, Gany A. Application of Activated Aluminum Powder for Generation of Hydrogen from Water. Int. J. Hydrogen Energy 2010; 35(20): 10898-904.
27. Ivanov VG, Safronov MN, Gavriluk OV. Macrokinetics of Oxidation of Ultradisperse Aluminum by Water in Liquid Phase. Combust., Explos. Shock Waves 2001; 37(2): 173-7.
28. Lyashko AP, Medvinskii AA, Savel'ev GG, Il'in AP, Yavorovskii NA. Specific Features of the Interaction of Submicron Aluminum Powders with Liquid Water: Makrokinetics, Products and Manifestation of Self Heating. Kinet. Catal. 1990; 31(1): 967-72.
29. Petrovic J, Thomas G. Reaction of Aluminum with Water to Produce Hydrogen. U.S. Department of Energy, 2008.

Chapter IV. Aluminum-water propellant experiments

The behavior of aluminum-water propellants containing different nano-size powders was investigated in order to study and characterize their properties. The propellants were prepared by mixing the aluminum powder with distilled water at an equivalence ratio of $\phi = 1$ between the water and the active aluminum. Equivalence ratio was determined according to the combustion reaction of pure aluminum and water (seen in Eq. 1), and is calculated to be 1:1 mass-wise between aluminum and water.



Three nano aluminum powders were examined: uncoated (U-ALEX, which includes the protective oxide layer), palmitic-acid coated (L-ALEX) and Viton coated (V-ALEX). Table 1 presents powder characteristics, including active aluminum analysis results. Figure 1 shows TEM images of all three powders, where the thin coating is visible in all images. In order to achieve good mixing, a surfactant (Rhodasurf, 3% with respect to water) was added to the hydrophobic L-ALEX and water mixture. In addition, ultrasonic agitation was employed in order to break and separate the heavily agglomerated V-ALEX during its mixing with water. All three water-powder mixtures were tested for reacting prematurely due to the close proximity between fuel (Al) and oxidizer in the propellant matrix. Hydrogen production with time was monitored for the mixtures, and negligible amounts were recorded throughout several hours (for the L-ALEX and V-ALEX) and 24 hour period (for U-ALEX).

Table 1: Nano-powders characteristics

	$d_{0.5}$ [nm]	Coating	Coating density [g/cm ³]	Active aluminum [% mass]
L-ALEX	120	Palmitic acid	0.85	87.9
V-ALEX	120	Viton	1.75-1.9	78.2
U-ALEX	120	Alumina	4	90

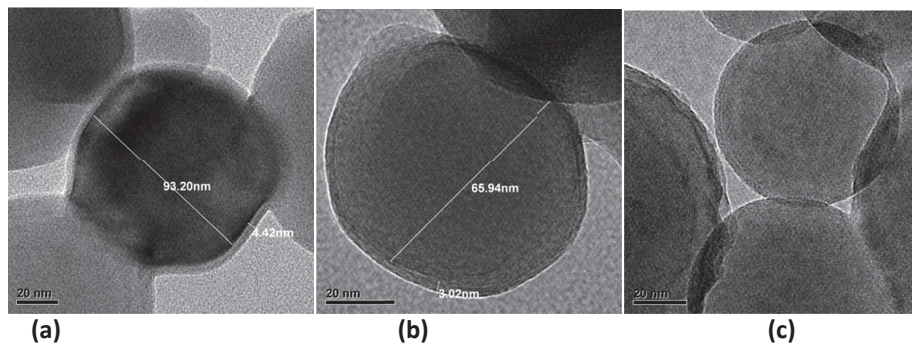


Figure 1: TEM images of L-ALEX (a), V-ALEX (b) and U-ALEX (c)

Propellant strands consisted of 9 mm inner diameter glass tubes, which Al-water mixtures were poured into, and were sealed in the bottom end by epoxy glue. Typically, each strand was 12-13 cm long and contained 9-10 grams of propellant. The strand was ignited by a small drop of Zr/iron oxide thermite which was dried around an electric ignition wire. Thin electrical wires were passed through the propellant 3.5" apart from one another, and served as the acquisition system's combustion start and finish, allowing the measurements of the burning time and burn rate. In each experiment three strands were mounted on the strand-burner head, enabling three burn rate measurements per shot. A schematic description of the Al-water strands is shown in Fig. 2a, and a picture of the strands mounted on the strand-burner head is shown in Fig. 2b. Experiments were conducted for propellants containing water and nano aluminum (either U-ALEX, V-ALEX or L-ALEX) at pressures varying from 1000 psi to 3500 psi.

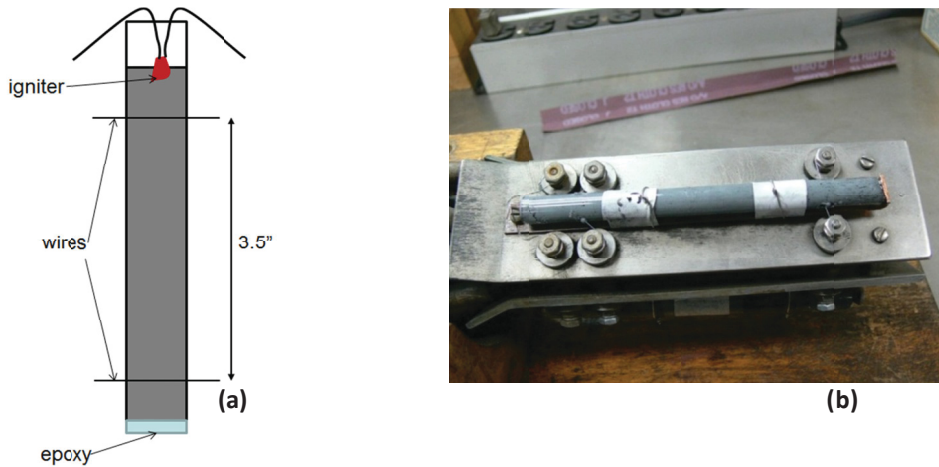


Figure 2: Al-water propellant strand schematics (a) and a real strand mounted on burner head (b)

Propellant density was measured for all strands prior to ignition. Figure 3 presents the density of the different strands. It can be seen that propellants containing L-ALEX powder possess lower density than the others, and that U-ALEX propellants generally have the highest density among the three. Average density was calculated for all three propellant types, and was found to be 1.22, 1.39 and 1.45 g/cm³ for the L-ALEX, V-ALEX and U-ALEX, respectively.

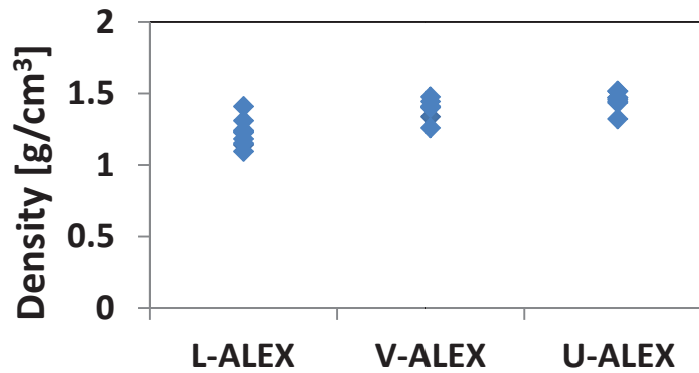


Figure 3: Propellant density of strands containing L-ALEX, V-ALEX or U-ALEX

Burn rate results are presented in Fig. 4. It can be seen that the experiments conducted at 3500 psi exhibit a notable drop in burn rate, compared to the results obtained for 2000 psi experiments. This trend does not comply with the well-known burn-rate behavior with pressure ($r = a \cdot P_c^n$). It is possible that this behavior is related to a combustion regime change due to the supercritical properties of water in these conditions. It seems that all three powders collapse to a burn-rate of approximately 12 mm/s in these conditions. The relatively high burn rates obtained at 2000 psi may also suggest that the classical description ($r = a \cdot P_c^n$) needs some revision for these pressures. Pressure exponent exceeds unity for some cases when these results are taken into account, a value that cannot represent truthfully a stable combustion. It is important to note that for both conventional composite propellants and ALICE (aluminum-ice) propellants, the burn rate power-law dependence of pressure was not valid for pressures higher than ~1800 psi, which means this could be the case in these experiments as well.

Another trend seen in Fig. 4 is the relatively plateau burn-rate pressure dependence for the V-ALEX propellant. This may be of great importance to the solid propellant community, which greatly favors low pressure-exponent propellants due to motor design issues (the need for constant thrust profile), as well as due to stability reasons.

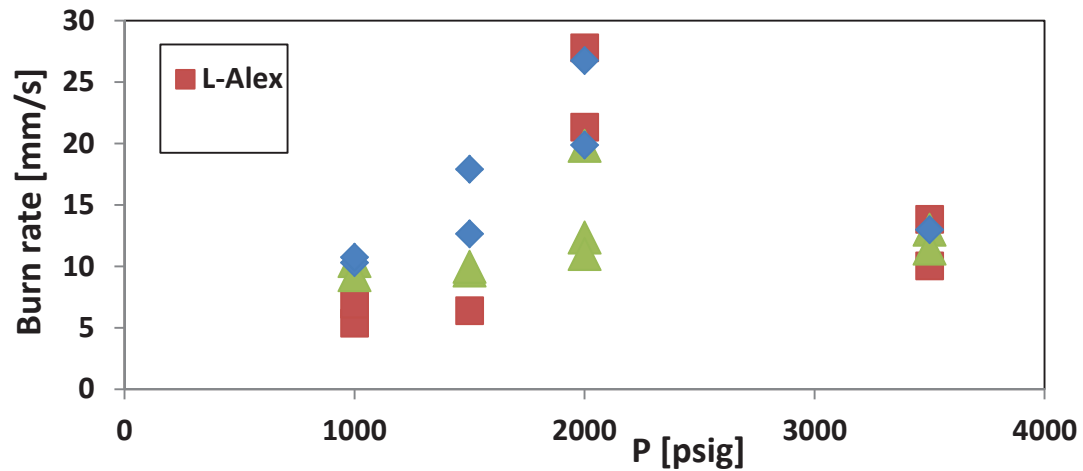


Figure 4: Burn rate of Al-water propellant strands vs. pressure

It is important to note, though, that as of now the relatively low number of experiments, as well as the large scatter in results prevents any conclusive inference with regards to the aluminum-water propellants behavior. Further tests and experiments have to be performed at a wide pressure range, and perhaps in various equivalence ratios, in order to reach decisive conclusions regarding this propellant.

Chapter V. Conceptual study of the light gas gun utilizing aluminum-water propellant

The main products of aluminum-water combustion are aluminum oxide and hydrogen gas. Although the adiabatic flame temperature is approximately 3000 K, at sufficiently high system pressures, the aluminum oxide remains in its condensed liquid phase. Therefore, the combustion reaction is capable of producing relatively pure high temperature hydrogen gas, which is an ideal propellant for a high speed gun. Experiments that are planned with supercritical water described in the above paragraph, will verify that the reaction rates are sufficient to produce large quantities of hydrogen within the timescale of the launch cycle. Nevertheless, it is a worthwhile exercise to evaluate the potential performance of a water-aluminum launcher.

It should be noted that a number of simplifying assumptions have been made for the purpose of providing a first order approximation of the potential performance of the water-aluminum launcher. The propellant is treated as an ideal gas, composed of pure non-dissociated hydrogen (specific heat ratio (γ) of 1.4, molecular weight (MW) of 2 kg/k-mol). All forms of losses have been neglected, including heat loss, gas friction, projectile friction, and projectile back-pressure.

Evaluating the theoretical performance of a pre-burnt propellant ideal gas gun (PPIG) allows us to gain insight into the main factors affecting gun performance. The ratio of the driving pressure over the initial pressure in a PPIG is given by Equation 1. The maximum theoretical velocity of a PPIG is given by Equation 2. Both equations show the need for having a high sound-speed (c_o) propellant.

$$\frac{p}{p_o} = \left(1 - \frac{\gamma-1}{2} \frac{u}{c_o}\right)^{\frac{2\gamma}{\gamma-1}} \quad (1)$$

$$u_{max} = \frac{2}{\gamma-1} c_o \quad (2)$$

The sound-speed of a propellant is given by Equation 3.

$$c = \sqrt{\frac{\gamma \bar{R} T}{MW}} \quad (3)$$

As can be seen, in order to maximize its sound-speed, a propellant should have a very high temperature and a very low molecular weight. The maximum launch cycle temperature is typically kept below 3000 K, in order to avoid excessive ablation damage to the gun. The molecular weight of the driver gas is dictated by the type of propellant being used, which is why heavy nitrocellulose (gun powder) propellants typically have relatively low performance capabilities. Although a number of light gas (hydrogen or helium) gun technologies exist, such as the two stage light gas gun, they typically require very large launchers and long set up times. A water-aluminum light gas gun would have the advantage of having a high temperature and low molecular weight propellant in a compact design, allowing it to reach velocities well above the capabilities of gun powder launchers in a similarly compact design.

A quasi-one-dimensional Lagrangian ballistics code has been developed in order to model the internal ballistics of a water-aluminum light gas gun. The code uses a second-order accurate numerical scheme developed by J. Von Neumann & R.D. Richtmyer (A Method for the Numerical Calculation of Hydrodynamic Shocks, 1950). The code has been validated against a number of analytical solutions, as well as published CFD data found in A. Seigel (The Theory of High Speed Guns, 1965). In order to perform the PPIG simulations, a chemical equilibrium code was used to determine the final composition, pressure, and temperature of the products.

PPIG (Pre-Burnt Propellant Gun Ideal Gas Gun Simulations) simulations were used as a first estimate of the performance of the water-aluminum light gas gun. A chemical equilibrium Russian code Thermo was used to determine the properties of the driver gas. The equilibrium simulation consisted of a constant volume reaction of water-aluminum in a 300 K vessel pressurized to 10 MPa with hydrogen. Zirconium dioxide was also included in the simulation to represent the high temperature filter which would be needed to prevent the liquid aluminum oxide from moving with the flow. The “realistic” simulated gas conditions are illustrated in Fig. 8.

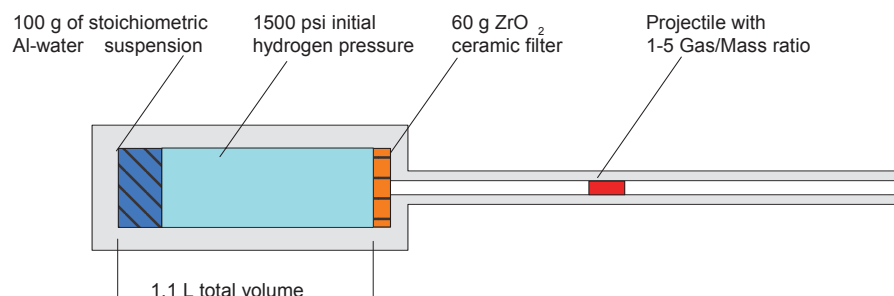


Figure 8: “Realistic” simulation parameters of aluminum-water light gas gun.

The initial and equilibrium compositions are shown in Table 1. As can be seen, molecular hydrogen (H_2) is the dominant gaseous species, indicating that treating the gas as pure hydrogen is a good estimate. The equilibrium temperature was of 2982 K, and the final pressure 69.3 MPa. Care was taken to ensure that the equilibrium gas pressure was not so high as to exceed what could be contained by a steel vessel.

Table 3: Initial and final compositions in the equilibrium code

Initial Composition		Final Composition		
Species	Moles	Species	Moles	Gaseous Molar Fraction
Al (s)	2	Al (g)	9.40E-04	0.01%
H_2O (l)	3	H_2O (g)	0.0132	0.18%
H_2 (g)	4.5	H_2 (g)	7.4755	99.47%
ZrO_2 (s)	0.5	ZrO_2 (l)	0.3342	N/A
		ZrO_2 (s)	0.1658	N/A
		H (g)	0.017	0.23%
		AlHO (g)	0.0024	0.03%
		Al_2O (g)	0.0031	0.04%
		AlH (g)	0.0025	0.03%
		AlH_2 (g)	3.45E-04	0.00%
		Al_2O_3 (l)	0.9937	N/A

Using the information from the chemical equilibrium software, PPIG simulations could be run to estimate the performance of the launcher. Figure 1 shows projectile velocity as a function of position (in calibers) for a number of different projectiles. The ratio of projectile mass (M) to driver gas mass (G), was varied from 1 to 5. Care was taken to choose realistic projectile aerial density values. In this case, the G/M of 5 projectile is equivalent to a 0.5 caliber long plastic projectile, while the G/M of 1 projectile is equivalent to a 2.5 caliber long plastic projectile. The figure indicates that for substantially large G/M ratios, velocities above 4 km/s are possible with reasonably long barrels and light projectiles. This is well above the capacity of powder guns, which are limited to approximately 2.5 km/s.

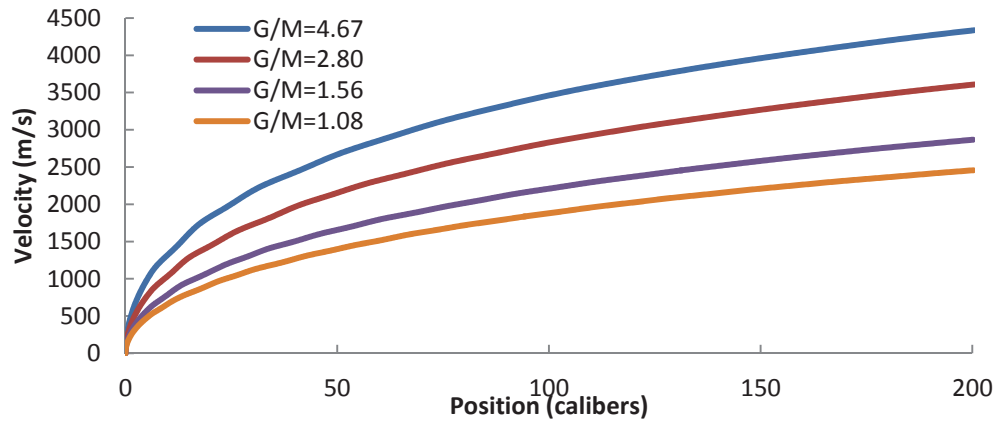


Figure 9: Projectile velocity as a function of position in calibers for a number of gas to projectile mass ratios

Although PPIG simulations give us some insight into the capabilities of the water-aluminum light gas gun, they are not an adequate design tool for a launcher. The performance of the launcher will depend strongly on the rate of production of high temperature hydrogen during the combustion reaction, which is not taken into account in a PPIG simulation.

Provided estimations show that a water-aluminum light gas gun has the potential reaching velocities well above the capabilities of conventional powder guns. Its design is expected to be much more compact than other light gas gun technologies and possibly suited for the field applications. In order to continue developing the launcher, the current Lagrangian ballistics code will need to be modified to incorporate a propellant burn rate model. This will allow the code to model a complete launch cycle, which incorporates the kinetics of the water-aluminum reaction. The reaction rates at high pressures and temperature typically encountered during the launch cycle are in the range above the water critical point. Thus the described in the previous paragraph (A2) planned work on supercritical aluminum oxidation will answer the question if the aluminum-water propellant light gas gun concept is realistic.